



Published in final edited form as:

*Immunity*. 2023 September 12; 56(9): 2021–2035.e8. doi:10.1016/j.immuni.2023.07.002.

## Ketolysis drives CD8<sup>+</sup> T cell effector function through effects on histone acetylation

Katarzyna M. Luda<sup>1,2,10</sup>, Joseph Longo<sup>1,10</sup>, Susan M. Kitchen-Goosen<sup>1</sup>, Lauren R. Duimstra<sup>1</sup>, Eric H. Ma<sup>1</sup>, McLane J. Watson<sup>1</sup>, Brandon M. Oswald<sup>1</sup>, Zhen Fu<sup>3</sup>, Zachary Madaj<sup>3</sup>, Ariana Kupai<sup>4</sup>, Bradley M. Dickson<sup>4</sup>, Lisa M. DeCamp<sup>1</sup>, Michael S. Dahabieh<sup>1</sup>, Shelby E. Compton<sup>1</sup>, Robert Teis<sup>1</sup>, Irem Kaymak<sup>1</sup>, Kin H. Lau<sup>3</sup>, Daniel P. Kelly<sup>5</sup>, Patrycja Puchalska<sup>6</sup>, Kelsey S. Williams<sup>1</sup>, Connie M. Krawczyk<sup>1</sup>, Dominique Lévesque<sup>7</sup>, François-Michel Boisvert<sup>7</sup>, Ryan D. Sheldon<sup>8</sup>, Scott B. Rothbart<sup>4</sup>, Peter A. Crawford<sup>6,9</sup>, Russell G. Jones<sup>1,11,\*</sup>

<sup>1</sup>Department of Metabolism and Nutritional Programming, Van Andel Institute, Grand Rapids, MI 49503, USA

<sup>2</sup>University of Copenhagen, Novo Nordisk Foundation Center for Basic Metabolic Research, Blegdamsvej 3B, 2200 København, Denmark

<sup>3</sup>Bioinformatics and Biostatistics Core, Van Andel Institute, Grand Rapids, MI 49503, USA

<sup>4</sup>Department of Epigenetics, Van Andel Institute, Grand Rapids, MI 49503, USA

<sup>5</sup>Cardiovascular Institute and Department of Medicine, Perelman School of Medicine at the University of Pennsylvania, Philadelphia, PA 19104, USA

<sup>6</sup>Department of Medicine, Division of Molecular Medicine, University of Minnesota, Minneapolis, MN 55455, USA

<sup>7</sup>Department of Anatomy and Cell Biology, Université de Sherbrooke, Sherbrooke, QC J1E 4K8, Canada

<sup>8</sup>Mass Spectrometry Core, Van Andel Institute, Grand Rapids, MI 49503, USA

<sup>9</sup>Department of Biochemistry, Molecular Biology, and Biophysics, University of Minnesota, Minneapolis, MN 55455, USA

<sup>10</sup>These authors contributed equally

\*Correspondance: Russell G. Jones, russell.jones@vai.org.

### Author Contributions

Conceptualization, KML and RGJ; Experimental Design, KML, JL, EHM, DPK, PP, CMK, FMB, RDS, SBR, PAC, and RGJ; Investigation, KML, JL, SMKG, LRD, EHM, MJW, BMO, AK, LMD, MSD, SC, RT, and IK; Data Analysis, KML, JL, SKMG, EHM, MJW, BMO, ZF, ZM, BMD, KHL, KSW, DL, RDS, and RGJ; Writing – Original Draft, KML, KSW, and RGJ; Writing – Editing, KML, JL, CMK, SBR, PAC, and RGJ; Visualization, ZF and KSW; Supervision, RGJ; Funding Acquisition, RGJ.

### Declaration of Interests

RGJ is a scientific advisor for Agios Pharmaceuticals and Servier Pharmaceuticals and is a member of the Scientific Advisory Board of Immunomet Therapeutics.

**Publisher's Disclaimer:** This is a PDF file of an unedited manuscript that has been accepted for publication. As a service to our customers we are providing this early version of the manuscript. The manuscript will undergo copyediting, typesetting, and review of the resulting proof before it is published in its final form. Please note that during the production process errors may be discovered which could affect the content, and all legal disclaimers that apply to the journal pertain.

<sup>11</sup>Lead contact

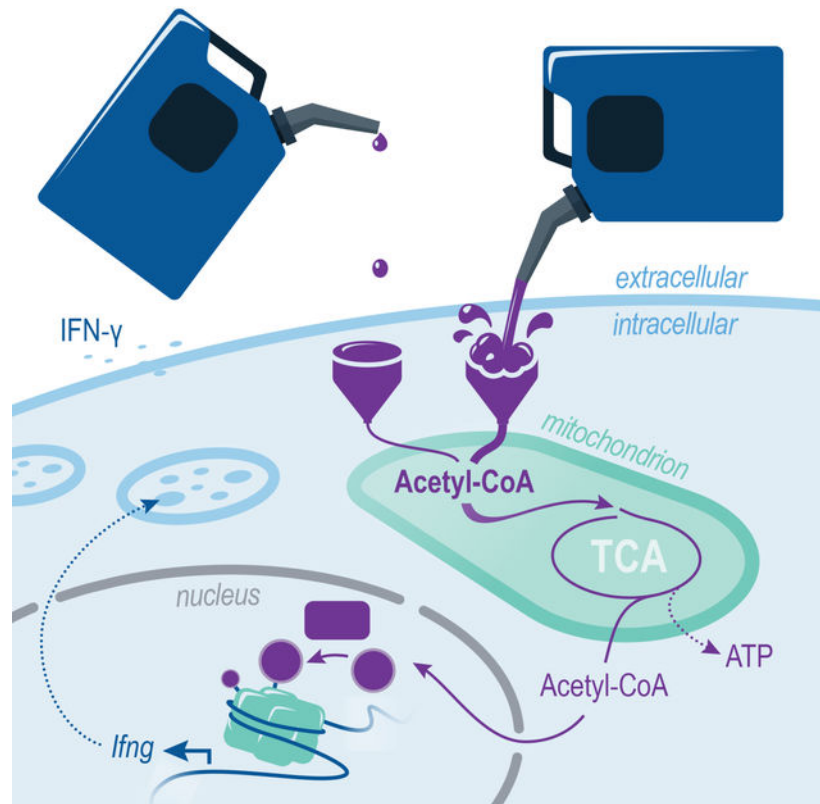
## Summary

Environmental nutrient availability influences T cell metabolism, impacting T cell function and shaping immune outcomes. Here, we identified ketone bodies (KBs) – including  $\beta$ -hydroxybutyrate ( $\beta$ OHB) and acetoacetate (AcAc) – as essential fuels supporting CD8<sup>+</sup> T cell metabolism and effector function.  $\beta$ OHB directly increased CD8<sup>+</sup> T effector (Teff) cell cytokine production and cytolytic activity, and KB oxidation (ketolysis) was required for Teff cell responses to bacterial infection and tumor challenge. CD8<sup>+</sup> Teff cells preferentially used KBs over glucose to fuel the tricarboxylic acid (TCA) cycle *in vitro* and *in vivo*. KBs directly boosted the respiratory capacity and TCA cycle-dependent metabolic pathways that fuel CD8<sup>+</sup> T cell function. Mechanistically,  $\beta$ OHB was a major substrate for acetyl-CoA production in CD8<sup>+</sup> T cells and regulated effector responses through effects on histone acetylation. Together, our results identify cell-intrinsic ketolysis as a metabolic and epigenetic driver of optimal CD8<sup>+</sup> T cell effector responses.

## eTOC Blurp

Environmental nutrient availability influences T cell function, yet the substrates that fuel T cell metabolism *in vivo* are poorly defined. Here, Luda and Longo *et al.* identify ketolysis (breakdown of ketone bodies) as a metabolic pathway required for optimal CD8<sup>+</sup> T cell effector function *in vivo*. Ketone bodies, including  $\beta$ OHB, are physiologic fuels for T cells, preferred over glucose for acetyl-CoA synthesis, and regulate effector function through effects on histone acetylation.

## Graphical Abstract



## Keywords

CD8<sup>+</sup> T cells; ketone bodies; ketolysis; metabolism; TCA cycle; effector function; cancer immunology; epigenetics; acetyl-CoA

## Introduction

Multicellular organisms have evolved protective strategies for defending against pathogens, such as viruses and bacteria, and intrinsic threats such as cancer. Central to host defense are CD8<sup>+</sup> T cells, which are critical for pathogen clearance and protecting the host from reinfection through long-lived immune memory<sup>1,2</sup>. One of the fundamental biological programs supporting T cell effector function is cellular metabolism, which generates energy and biosynthetic precursors essential for CD8<sup>+</sup> T effector (Teff) cell proliferation, survival, and production of effector molecules (i.e., IFN- $\gamma$ , TNF- $\alpha$ , and cytolytic factors)<sup>3–5</sup>. CD8<sup>+</sup> Teff cells undergo extensive metabolic rewiring to arm themselves with the bioenergetic and biosynthetic capacity to successfully protect the host<sup>6,7</sup>. However, Teff cell function is highly dependent on nutrient availability<sup>8–11</sup>, which in the whole organism is governed by diet and host metabolism. Changes in host metabolic homeostasis triggered by infection, including catabolic wasting (“cachexia”) and anorexia, can influence the pathogenesis of the infection and affect disease tolerance<sup>12,13</sup>. In response to bacterial or viral infection, disrupted feeding behavior and metabolic rewiring in tissues, such as the liver, promote changes in host metabolism including lipolysis and the production of ketone bodies

(KBs)<sup>14–17</sup>; however, how T cell-intrinsic metabolic programming synergizes with changes in host metabolism during an immune response remains poorly defined.

In this study, we identified KB metabolism as a prominent feature of highly functional CD8<sup>+</sup> Teff cells and demonstrated that circulating KB concentrations are elevated in response to *Listeria* infection. KB availability enhanced CD8<sup>+</sup> T cell effector function, raising the possibility that KB metabolism influences T cell-mediated immunity. In line with this hypothesis, we report that genetic perturbation of KB oxidation (ketolysis) in CD8<sup>+</sup> T cells impairs effector responses to bacterial infection and cancer. Using metabolic tracers, we showed that CD8<sup>+</sup> Teff cells preferentially used KBs over glucose to fuel acetyl-CoA-dependent metabolic processes *in vitro* and *in vivo*, and that KB-derived acetyl-CoA regulated effector responses through effects on histone acetylation. Taken together, our data establish CD8<sup>+</sup> T cell-intrinsic ketolysis as a non-redundant, physiologic regulator of T cell functionality.

## Results

### Ketolysis is a metabolic feature of functional CD8<sup>+</sup> T effector (Teff) cells

Effective control of infection and cancer growth requires robust effector CD8<sup>+</sup> T cell responses, which are driven by T cell receptor (TCR)-dependent transcriptional, epigenetic, and metabolic programs<sup>2,18–20</sup>. To define features of highly functional CD8<sup>+</sup> T effector (Teff) cells in the context of both infection and cancer, we conducted a meta-analysis of three independent studies characterizing gene expression profiles of CD8<sup>+</sup> T cells responding to acute infection (*Listeria monocytogenes* (*Lm*) or lymphocytic choriomeningitis virus (LCMV), Armstrong strain), chronic infection (LCMV, Clone-13 strain), or syngeneic tumors<sup>21–23</sup>. Pearson correlations (Fig. 1A) and PCA among samples revealed clustering of samples into 6 main T cell subsets: 1) naïve (Tn), 2) Teff, 3) memory (Tmem), 4) early cancer exhausted (Tex), 5) late cancer Tex, and 6) chronic virus Tex cells. To identify genes preferentially associated with “functional” versus “dysfunctional” CD8<sup>+</sup> T cells, we compared gene expression patterns between Teff cells and late cancer- or chronic viral-driven Tex cells (Table S1). Wald test statistics for each gene were generated for each pairwise comparison (tumor and viral datasets) and median scores were used to identify genes associated with functional versus dysfunctional states (Fig. 1B). Rank analysis revealed that genes associated with CD8<sup>+</sup> T cell cytotoxicity (i.e., *Klrg1*, *Klf2*, *Rora*, *Lef1*) were enriched in the functional Teff cell cohort, while dysfunctional CD8<sup>+</sup> T cells displayed enrichment in genes associated with T cell exhaustion (i.e., *Tox*, *Pdcd1*, *Entpd1*, *Lag3*) (Fig. 1B, Fig. S1A, Table S1) and inflammatory signaling (Fig. S1B). Given the central role of metabolism in supporting Teff cell responses<sup>6,24</sup>, we hypothesized that specific metabolic pathways may contribute to CD8<sup>+</sup> Teff cell function. KEGG pathway analysis of the top ~4% of genes expressed by functional CD8<sup>+</sup> Teff cells revealed enrichment of several metabolic pathways (Fig. 1C). Among these, the synthesis and degradation of ketone bodies (KBs) was the most highly enriched metabolic pathway in functional CD8<sup>+</sup> T cells (Fig. 1C).

KBs, including  $\beta$ -hydroxybutyrate ( $\beta$ OHB) and acetoacetate (AcAc), are metabolic fuels critical for supporting bioenergetic metabolism during periods of nutrient deprivation<sup>25–27</sup>.

KBs can also have fates beyond terminal oxidation, including impact on cell signaling, direct and indirect effects on histone post-translational modifications, and inhibition of inflammatory processes<sup>27,28</sup>. The primary site of KB production in mammals is the liver, which generates AcAc and  $\beta$ OHB from fatty acid-derived acetyl-CoA. KBs are subsequently transported to extrahepatic tissues for terminal oxidation in the tricarboxylic acid (TCA) cycle. KBs are metabolized to acetyl-CoA through a set of enzymatic reactions collectively called ketolysis. Mitochondrial  $\beta$ OHB dehydrogenase (BDH1) converts D- $\beta$ OHB to AcAc, which is in turn converted to acetoacetyl-CoA by succinyl-CoA-3-oxaloacid CoA transferase (SCOT, encoded by the *OXCT* genes) (Fig. 1D). Acetoacetyl-CoA is further processed by thiolase acetyl-CoA acetyltransferase (ACAT) to generate two molecules of acetyl-CoA, which can enter the TCA cycle (Fig. 1D). Gene expression analysis of CD8<sup>+</sup> T cells responding to *Lm* infection<sup>29</sup> revealed increased expression of mRNA transcripts encoding several ketolytic enzymes (i.e., *Bdh1*, *Oxct1*, *Acat1/2*) in Teff cells relative to Tn and Tmem cells (Fig. 1D). Analysis of publicly-available proteomics data<sup>30</sup> revealed a ~2–3-fold induction in *Bdh1* and *Scot* expression in CD8<sup>+</sup> Teff cells following *in vitro* activation (Fig. S1C), while proteomics analysis of CD8<sup>+</sup> Teff cells responding to *Lm* infection *in vivo*<sup>31</sup> revealed greater *Bdh1* expression in Teff cells compared to Tn cells at both 2.5 and 6 days post-infection (dpi) (Fig. S1D, Table S2). Thus, the transition from Tn to Teff cell states is associated with increased expression of ketolytic enzymes.

We next asked if KBs could directly impact CD8<sup>+</sup> Teff cell function. CD8<sup>+</sup> Teff cells activated in the presence of  $\beta$ OHB displayed increased capacity to produce IFN- $\gamma$ , reflected by both an increased percentage of IFN- $\gamma$ -producing cells and increased IFN- $\gamma$  protein expression per cell (as determined by increased mean fluorescence intensity (MFI) of IFN- $\gamma$  staining) (Fig. 1E). We recently developed a modified cell culture medium denoted VIM that more closely mimics the polar metabolite concentrations in mouse serum<sup>32</sup>. We reported that activating CD8<sup>+</sup> T cells in VIM supplemented with additional physiologic carbon sources (PCS; acetate,  $\beta$ OHB, citrate, lactate, pyruvate) enhances their effector function, including IFN- $\gamma$  and granzyme production<sup>32</sup>. Removing  $\beta$ OHB from PCS-supplemented VIM reduced IFN- $\gamma$  production by CD8<sup>+</sup> T cells (Fig. S1E), suggesting that  $\beta$ OHB is an active component of PCS responsible for enhancing IFN- $\gamma$  production. Indeed, CD8<sup>+</sup> T cells activated in VIM supplemented with  $\beta$ OHB alone displayed increased IFN- $\gamma$  and TNF- $\alpha$  production in a concentration-dependent manner (Figs. 1F–G, S1E–F), while CD8<sup>+</sup> T cell proliferation and expression of activation markers were unaffected by  $\beta$ OHB up to 5 mM (Figs. 1H, S1G). Collectively, these data support that ketolysis is a metabolic feature of CD8<sup>+</sup> Teff cells and  $\beta$ OHB can increase cytokine production by CD8<sup>+</sup> T cells.

### CD8<sup>+</sup> T cell-intrinsic ketolysis is required for optimal effector function

Next, we assessed whether the effects of  $\beta$ OHB on IFN- $\gamma$  production by CD8<sup>+</sup> T cells were dependent on oxidation of  $\beta$ OHB via ketolysis. We crossed *Bdh1*-floxed mice<sup>33</sup> to *Cd4-Cre* transgenic mice to generate a mouse model with conditional deletion of *Bdh1* in mature T cells (Fig. S2A). *Bdh1*<sup>-/-</sup> CD8<sup>+</sup> Teff cells displayed reduced IFN- $\gamma$  production relative to control cells following *in vitro* activation (Fig. 2A), and *Bdh1* was required for the  $\beta$ OHB-driven increase in IFN- $\gamma$  production by CD8<sup>+</sup> Teff cells (Fig. 2B), indicating that  $\beta$ OHB

augments IFN- $\gamma$  production via T cell-intrinsic ketolysis. Despite being compromised in their ability to produce cytokines, CD8<sup>+</sup> Teff cell proliferation was unaffected by *Bdh1* deletion (Fig. 2C).

We next assessed the role of ketolysis in CD8<sup>+</sup> Teff cell function *in vivo* following infection with recombinant strains of *Lm* that express ovalbumin (*Lm*-OVA), which induce robust expansion of IFN- $\gamma$ -producing CD8<sup>+</sup> T cells *in vivo*<sup>34</sup>. Infection of wild type mice with an attenuated strain of *Lm*-OVA resulted in elevated  $\beta$ OHB in the serum, liver, and spleen 2 dpi, with an average circulating  $\beta$ OHB concentration of ~1 mM (Fig. 2D). We therefore used *Lm*-OVA to interrogate the role of cell-intrinsic ketolysis in IFN- $\gamma$  production by CD8<sup>+</sup> Teff cells *in vivo*. Given that both  $\beta$ OHB and AcAc are present in circulation<sup>27</sup> and that the ketolytic enzymes required to oxidize both  $\beta$ OHB and AcAc are expressed by Teff cells (Fig. 1D, S1C–D), we generated ketolysis-deficient CD8<sup>+</sup> T cells via shRNA-mediated silencing of *Oxct1* in *Bdh1*<sup>-/-</sup> cells (Fig. 2E, S2A). OVA-specific OT-I control or *Bdh1*<sup>-/-</sup> CD8<sup>+</sup> T cells were transduced with a control (shFF, targeting firefly luciferase) or *Oxct1*-targeting shRNA and transferred into congenic hosts. Mice were subsequently infected with attenuated *Lm*-OVA and CD8<sup>+</sup> Teff cell responses were analyzed 7 dpi (Fig. S2B–D). Ketolysis-deficient OT-I CD8<sup>+</sup> T cells displayed increased expansion *in vivo* (Fig. S2C), but no major defect in their ability to differentiate into effector or memory precursor subsets (Fig. S2D). Consistent with our *in vitro* observations (Fig. 1E–F), ketolysis-deficient CD8<sup>+</sup> T cells displayed lower IFN- $\gamma$  production *in vivo* compared to control cells (Fig. 2F). However, ketolysis-deficient CD8<sup>+</sup> T cells were able to differentiate into memory cells and responded similarly upon rechallenge 45 dpi with a virulent strain of *Lm*-OVA (Fig. S2E–H).

To identify the molecular mechanisms by which ketolysis impacts CD8<sup>+</sup> T cell effector function, we performed RNA sequencing (RNA-seq) of control and ketolysis-deficient OT-I CD8<sup>+</sup> T cells isolated from the spleens of attenuated *Lm*-OVA-infected mice 7 dpi (Table S3, Fig. S2I). Pathway analysis revealed enrichment of proliferative programs (i.e., cell cycle, E2F targets)—consistent with increased expansion of ketolysis-deficient OT-I cells *in vivo* (Fig. S2C)—and a loss of inflammatory signatures (i.e., IFN- $\alpha$ /IFN- $\gamma$  response, allograft rejection) in ketolysis-deficient T cells (Fig. S2J). GSEA using T cell exhaustion gene signatures from chronic LCMV-infected mice (Table S4)<sup>35</sup> revealed that ketolysis-deficient T cells displayed transcriptional features of early effector exhausted (Tex<sup>eff</sup>) T cells, which are associated with initiation of the molecular exhaustion program<sup>35</sup> (Fig. 2G). In contrast, control cells displayed signatures of conventional Teff cells and “self-renewing” progenitor exhausted (Tex<sup>prog</sup>) T cells (Fig. 2G). Moreover, using gene signatures derived from single-cell profiling of human T cells (Table S4)<sup>36</sup>, we observed a loss of CD8<sup>+</sup> T cell cytotoxicity signatures in ketolysis-deficient T cells (Fig. 2H). Consistent with these analyses, *Bdh1*<sup>-/-</sup> CD8<sup>+</sup> T cells displayed a 30–40% reduction in their ability to lyse MC38-OVA cancer cells *in vitro* (Fig. 2I), and MC38-OVA tumors displayed accelerated growth in *Bdh1*<sup>fl/fl</sup> *Cd4-Cre* mice (Fig. 2J–K). Collectively, these findings implicate cell-intrinsic ketolysis in the development of CD8<sup>+</sup> T cell functional programs required for cytolytic function and tumor control.

## KBs fuel the TCA cycle in CD8<sup>+</sup> T cells

Given that KBs play critical roles in organismal energy homeostasis, including serving as oxidative fuels during states of low nutrient availability<sup>27</sup>, we questioned whether KBs function as a fuel source for CD8<sup>+</sup> T cells. Using <sup>13</sup>C-based metabolic tracers, we found that [U-<sup>13</sup>C<sub>4</sub>]-βOHB was readily imported by proliferating Teff cells, saturating the intracellular βOHB pool within 2 minutes of exposure (Fig. 3A, S3A). While previous work suggests that CD8<sup>+</sup> Tmem cells can undergo ketogenesis<sup>37</sup>, rapid and near complete <sup>13</sup>C enrichment of the βOHB pool from [U-<sup>13</sup>C<sub>4</sub>]-βOHB suggested the absence of ketogenesis from endogenous substrates in Teff cells, which would have diluted the total βOHB pool with unlabeled βOHB. Furthermore, we did not observe contribution of [U-<sup>13</sup>C<sub>6</sub>]-glucose to intracellular βOHB in Teff cells (Fig. 3A).

To compare the contribution of KB-derived carbon with other carbon sources for TCA cycle metabolism, we cultured CD8<sup>+</sup> Teff cells in the presence of <sup>13</sup>C-labeled substrates at concentrations commonly observed in plasma<sup>38,39</sup> and assessed their contribution to TCA cycle-derived metabolites. Of all <sup>13</sup>C-labeled substrates, [U-<sup>13</sup>C<sub>4</sub>]-βOHB-derived carbon was the most highly enriched in TCA cycle intermediates (Fig. 3B), contributing to the citrate (M+2) pool 5-fold more than [U-<sup>13</sup>C<sub>6</sub>]-glucose (Fig. S3B), indicating that βOHB can contribute to TCA cycle metabolism even under nutrient-replete conditions.

We continued our *in vitro* studies using KBs at 2 mM (unless stated otherwise) to mimic circulating βOHB concentrations achieved with therapeutic ketogenic diets<sup>40,41</sup>. Both [U-<sup>13</sup>C<sub>4</sub>]-βOHB and [U-<sup>13</sup>C<sub>4</sub>]-AcAc contributed to citrate and malate synthesis, even in the presence of 5 mM glucose (Fig. 3C). Of note, the ratio of malate (M+2) to citrate (M+2) labeling from [U-<sup>13</sup>C<sub>4</sub>]-βOHB was approximately 0.5, indicative of “non-canonical” TCA cycle activity (i.e., the citrate-malate shuttle)<sup>42</sup> and potential use of citrate for other reactions beyond the TCA cycle (i.e., export to the cytosol for acetyl-CoA production). To assess direct competition between glucose and βOHB for TCA cycle metabolism, we designed a co-labeling experiment where activated CD8<sup>+</sup> Teff cells were cultured with [U-<sup>13</sup>C<sub>6</sub>]-glucose and [2,4-<sup>13</sup>C<sub>2</sub>]-βOHB. In this setting, metabolic intermediates generated during the first turn of the TCA cycle would be labeled M+1 from βOHB and M+2 from glucose (Fig. 3D). As expected, <sup>13</sup>C-labeled lactate (M+3) was generated exclusively from [U-<sup>13</sup>C<sub>6</sub>]-glucose (Fig. 3D); however, βOHB contributed approximately 50% more carbon to the synthesis of TCA cycle intermediates—particularly citrate—compared to glucose, despite being at lower molar concentration (Fig. 3D). Reducing the concentration of βOHB in culture revealed that [U-<sup>13</sup>C<sub>6</sub>]-glucose and [2,4-<sup>13</sup>C<sub>2</sub>]-βOHB contributed equally to citrate production at βOHB concentrations as low 200 μM (Fig. 3E). Moreover, βOHB contribution to citrate, malate, and aspartate production exceeded that of glucose at concentrations of 0.5–1 mM βOHB (Figs. 3E–F, S3C), which is well within the βOHB concentrations observed in serum of *Lm*-OVA-infected mice (Fig. 2D). Collectively, these data confirm that KBs are metabolic substrates for CD8<sup>+</sup> T cells, and that βOHB is preferentially used by CD8<sup>+</sup> T cells over glucose to fuel TCA cycle metabolism, even when glucose is abundant.

Given the contribution of βOHB and AcAc to TCA cycle metabolism, we next examined the impact of KB metabolism on T cell bioenergetics. Short-term exposure (2 h) of activated CD8<sup>+</sup> Teff cells to βOHB modestly increased their basal oxygen consumption rate (OCR)

and ATP production from OXPHOS (Fig. 3G, S3D). However, the maximal respiratory rate of CD8<sup>+</sup> T cells was greatly increased by KBs (2-fold and 1.5-fold increases for  $\beta$ OHB and AcAc, respectively), which corresponded to an increase in their maximal ATP production rate from OXPHOS (Fig. 3G–H). We also observed a slight increase in extracellular acidification rate (ECAR) and maximal glycolytic ATP production in CD8<sup>+</sup> T cells cultured with  $\beta$ OHB, but less so in cells cultured with AcAc (Fig. S3E–F). Collectively, these data indicate that KBs directly augment mitochondrial ATP production by boosting maximal respiratory capacity.

### $\beta$ OHB is a physiologic fuel for CD8<sup>+</sup> T cells

To confirm that CD8<sup>+</sup> T cells use  $\beta$ OHB as a fuel when responding to infection, we conducted *ex vivo* <sup>13</sup>C tracing experiments in which OT-I CD8<sup>+</sup> T cells isolated from *Lm*-OVA-infected mice (7 dpi) were subjected to short-term culture in VIM containing [U-<sup>13</sup>C<sub>6</sub>]-glucose and [2,4-<sup>13</sup>C<sub>2</sub>]- $\beta$ OHB. Like *in vitro*-activated T cells, *Lm*-OVA-specific T cells isolated 7 dpi readily oxidized  $\beta$ OHB in the TCA cycle (Fig. 4A). *Lm*-OVA-specific OT-I cells converted [2,4-<sup>13</sup>C<sub>2</sub>]- $\beta$ OHB to citrate, malate, and aspartate even at  $\beta$ OHB concentrations up to 20-fold lower than glucose (i.e., 200  $\mu$ M versus 5 mM) (Fig. 4B–C, S4A). Finally, we used *in vivo* <sup>13</sup>C metabolite infusions to evaluate  $\beta$ OHB utilization by CD8<sup>+</sup> T cells *in vivo*. We transferred Thy1.1<sup>+</sup> OT-I CD8<sup>+</sup> T cells into congenic recipient mice, infected the mice with attenuated *Lm*-OVA one day later, and then infused the mice for 2 h at 2 dpi (during proliferative expansion) or 6 dpi (peak of T cell response) with [U-<sup>13</sup>C<sub>4</sub>]- $\beta$ OHB or [U-<sup>13</sup>C<sub>6</sub>]-glucose prior to CD8<sup>+</sup> T cell isolation and metabolomic analysis (Fig. 4D)<sup>31,43</sup>. With our [U-<sup>13</sup>C<sub>4</sub>]- $\beta$ OHB infusion strategy, we achieved ~75% enrichment of fully-labeled (M+4) <sup>13</sup>C- $\beta$ OHB in circulation at both 2 and 6 dpi (Fig. S4B–C), with serum  $\beta$ OHB reaching similar concentrations as those observed in ketogenic diet settings (~2 mM). Moreover, we detected M+4 <sup>13</sup>C- $\beta$ OHB in *Lm*-OVA-specific CD8<sup>+</sup> T cells after only 2 h of infusion (Fig. S4B), corresponding to ~80–85% labeling of the total  $\beta$ OHB pool (Fig. 4E), indicating rapid import of  $\beta$ OHB by T cells *in vivo*. While we achieved good enrichment (~40%) of fully-labeled (M+6) <sup>13</sup>C-glucose in the circulating glucose pool (Fig. S4D), we observed no contribution of glucose to  $\beta$ OHB production in T cells (Fig. 4E) or circulating  $\beta$ OHB (Fig. S4E). Consistent with our *ex vivo* tracing results (Fig. 4A), infused [U-<sup>13</sup>C<sub>4</sub>]- $\beta$ OHB readily labeled TCA cycle-derived metabolites in *Lm*-OVA-specific CD8<sup>+</sup> T cells *in vivo* (Fig. 4F). Higher-order labeling patterns for [U-<sup>13</sup>C<sub>4</sub>]- $\beta$ OHB in citrate (i.e., M+3, M+4) suggested that  $\beta$ OHB carbon contributed to several turns of the TCA cycle within the short 2 h infusion period (Fig. 4G). Finally, we observed several key trends when we compared *in vivo* utilization of [U-<sup>13</sup>C<sub>4</sub>]- $\beta$ OHB to [U-<sup>13</sup>C<sub>6</sub>]-glucose by CD8<sup>+</sup> T cells. When normalized to steady-state <sup>13</sup>C-tracer enrichment in serum, both  $\beta$ OHB and glucose displayed similar contribution of <sup>13</sup>C to the TCA cycle (M+2 citrate, malate, and aspartate) during early T cell expansion *in vivo* (2 dpi); however, while glucose utilization by T cells declined by the peak of the T cell response to *Lm*-OVA (6 dpi), [U-<sup>13</sup>C<sub>4</sub>]- $\beta$ OHB still readily labeled intermediates of the TCA cycle (Fig. S4F), suggesting preferred use of  $\beta$ OHB as a TCA cycle fuel during the peak effector phase of the T cell response. Collectively, these data indicate that  $\beta$ OHB is a preferred fuel for CD8<sup>+</sup> T cells both *in vitro* and *in vivo* during an active immune response, even when glucose is available.

### BDH1 mediates the bioenergetic effects of ketolysis in CD8<sup>+</sup> T cells

The bioenergetic potential of KBs comes from both the dehydrogenation of  $\beta$ OHB to AcAc by *Bdh1*, which directly generates NADH, and the production of acetyl-CoA that can enter the TCA cycle and fuel downstream ATP production (Fig. 5A). Concordantly, we found that *Bdh1* was required for processing [U-<sup>13</sup>C<sub>4</sub>]- $\beta$ OHB, but not [U-<sup>13</sup>C<sub>4</sub>]-AcAc, into citrate (Fig. 5B). As expected, targeting the downstream ketolytic enzyme Scot (via silencing of *Oxct1*) diminished production of citrate from both [U-<sup>13</sup>C<sub>4</sub>]- $\beta$ OHB and [U-<sup>13</sup>C<sub>4</sub>]-AcAc (Fig. 5C). Using a Seahorse Bioanalyzer, we observed that both the increased respiratory capacity (Fig. 5D) and  $\beta$ OHB-induced boost in ATP production from OXPHOS (Figs. 5E, S5A) were dependent on *Bdh1*, but not on Scot;  $\beta$ OHB was still able to increase ATP production from OXPHOS in sh*Oxct1*-expressing T cells (Fig. 5E).  $\beta$ OHB also increased glycolytic ATP production in a *Bdh1*-dependent manner (Fig. S5B). Collectively, these data indicate that, in CD8<sup>+</sup> Teff cells, *Bdh1* is a critical regulator of both NADH production for OXPHOS and citrate synthesis for downstream metabolic reactions.

### $\beta$ OHB is the major substrate for acetyl-CoA production in CD8<sup>+</sup> T cells

Given our results that ketolysis can fuel CD8<sup>+</sup> T cell metabolism, we hypothesized that the contribution of KBs to acetyl-CoA production and mitochondrial metabolism may underlie their effects on T cell function. To test this hypothesis, we used sh*Oxct1*-expressing CD8<sup>+</sup> T cells to identify metabolic pathways downstream of ketolysis, as Scot activity is required for both  $\beta$ OHB and AcAc to enter the TCA cycle as acetyl-CoA (Fig. 5). Using the competitive [U-<sup>13</sup>C<sub>6</sub>]-glucose and [2,4-<sup>13</sup>C<sub>2</sub>]- $\beta$ OHB co-labeling strategy outlined in Fig. 3D, we observed reduced  $\beta$ OHB incorporation into TCA cycle intermediates, as well as acetyl-CoA (M+1) and downstream M+1 acetylated metabolites (i.e., Ac-spermidine, Ac-methionine) in sh*Oxct1*-expressing CD8<sup>+</sup> T cells (Fig. S6A), mechanistically linking ketolysis to acetyl-CoA production in T cells.

To further characterize the metabolic substrates contributing to acetyl-CoA production, we cultured activated CD8<sup>+</sup> T cells in VIM supplemented with PCS and individually traced uniformly <sup>13</sup>C-labeled fuels at their physiologic concentrations (as in Fig. 3B)<sup>32</sup>. Over 50% of the intracellular acetyl-CoA (M+2) pool was derived from [U-<sup>13</sup>C<sub>4</sub>]- $\beta$ OHB, compared to less than 10% from [U-<sup>13</sup>C<sub>6</sub>]-glucose (Fig. 6A). The production of acetyl-CoA from  $\beta$ OHB was dependent on cell-intrinsic ketolysis, as [U-<sup>13</sup>C<sub>4</sub>]- $\beta$ OHB-dependent acetyl-CoA (M+2) synthesis was decreased in ketolysis-deficient (sh*Oxct1*-expressing *Bdh1*<sup>-/-</sup>) T cells (Fig. 6B). Deletion of *Bdh1* in CD8<sup>+</sup> T cells did not significantly alter the intracellular pool size of acetyl-CoA (Fig. 6C); however, the distribution of contributing carbon sources to the acetyl-CoA pool was altered in *Bdh1*<sup>-/-</sup> T cells (Fig. 6D). While  $\beta$ OHB was the predominant contributor to intracellular acetyl-CoA (M+2) production in control cells, we observed increased contribution of [U-<sup>13</sup>C<sub>2</sub>]-acetate and [U-<sup>13</sup>C<sub>6</sub>]-glucose to acetyl-CoA (M+2) in *Bdh1*<sup>-/-</sup> T cells (Fig. 6D). Notably, these effects were not due to reduced intracellular  $\beta$ OHB availability, as *Bdh1*<sup>-/-</sup> CD8<sup>+</sup> T cells had a greater  $\beta$ OHB pool size compared to control cells (Fig. S6B).

Further analysis revealed that [U-<sup>13</sup>C<sub>4</sub>]- $\beta$ OHB-dependent acetylation of intracellular metabolites, including Ac-carnitine, were reduced in both *Bdh1*<sup>-/-</sup> (Fig. 6E) and sh*Oxct1*-

expressing (Fig. 6F) CD8<sup>+</sup> T cells. We also observed [U-<sup>13</sup>C<sub>4</sub>]-βOHB-derived Ac-carnitine (M+2) in CD8<sup>+</sup> T cells from *Lm*-OVA-infected animals infused with [U-<sup>13</sup>C<sub>4</sub>]-βOHB at 6 dpi (Fig. 6G), providing evidence that βOHB is used to generate acetyl-CoA in T cells *in vivo*. Finally, we examined whether βOHB was used for *de novo* fatty acid synthesis, one of the critical biosynthetic pathways supported by cytosolic acetyl-CoA in proliferating cells<sup>44,45</sup>. Consistent with the high contribution of βOHB to the acetyl-CoA pool in T cells (Fig. 6A), we found that [U-<sup>13</sup>C<sub>4</sub>]-βOHB carbon was incorporated into palmitate in a *Bdh1*-dependent manner (Fig. 6H), and that [U-<sup>13</sup>C<sub>4</sub>]-βOHB was preferred over [U-<sup>13</sup>C<sub>6</sub>]-glucose for palmitate synthesis in CD8<sup>+</sup> T cells (Fig. S6C). Collectively, these results establish βOHB as a major, and previously unappreciated, substrate for acetyl-CoA synthesis in CD8<sup>+</sup> T cells.

### βOHB alters histone acetylation in CD8<sup>+</sup> T cells

We next investigated the mechanistic impact of βOHB-dependent acetyl-CoA production on CD8<sup>+</sup> Teff cell function. Consistent with the effect of βOHB boosting IFN-γ production by CD8<sup>+</sup> T cells (Figs. 1E–F), we found that CD8<sup>+</sup> T cells activated in the presence of 5 mM βOHB displayed increased *Ifng* mRNA in a *Bdh1*-dependent manner (Fig. 7A). Ketolysis-deficient CD8<sup>+</sup> T cells cultured *in vitro* displayed reduced expression of mRNAs coding for IFN-γ (*Ifng*) and the cytotoxic protein Granzyme B (*Gzmb*) (Fig. 7B). Similarly, ketolysis-deficient CD8<sup>+</sup> Teff cells responding to attenuated *Lm*-OVA displayed reduced expression of several effector-associated genes (i.e., *Gzmk*, *Gzma*, *Cx3cr1*, *Klrg1*) at 7 dpi (Fig. 7C), correlating with their reduced cytotoxicity signature *in vivo* (Fig. 2H). Together, these data indicate that KBs impact Teff cell function, in part, through transcriptional regulation of effector genes.

Chromatin remodeling following T cell activation helps to stabilize effector gene expression and reinforce CD8<sup>+</sup> T cell effector functions<sup>20,24</sup>. Histone lysine (K) acetylation—specifically acetylation of lysine 27 on histone H3 (H3K27Ac)—is associated with chromatin accessibility and transcriptional activation<sup>46</sup>, and is important for effector gene expression by CD8<sup>+</sup> T cells<sup>47</sup>. Immunoblotting of isolated histones revealed reduced global histone H3 lysine acetylation in activated ketolysis-deficient CD8<sup>+</sup> T cells (Fig. 7D). In addition, treatment of *in vitro*-activated CD8<sup>+</sup> T cells with βOHB was sufficient to globally increase histone H3 acetylation at several lysine residues compared to controls, including H3K14Ac and H3K27Ac (Fig. 7E, S7A). βOHB has been implicated in epigenetic programming through its activity as a class I histone deacetylase (HDAC) inhibitor or through direct β-hydroxybutyrylation of histones<sup>48,49</sup>. However, the effect of βOHB on H3K27Ac was reduced in *Bdh1*<sup>-/-</sup> T cells (Fig. 7F), suggesting that ketolysis directly promotes changes in histone acetylation.

Given the major contribution of βOHB to the acetyl-CoA pool in CD8<sup>+</sup> T cells (Fig. 6A), we hypothesized that βOHB-derived acetyl-CoA was being used to acetylate histones. To test this directly, we cultured *in vitro*-activated CD8<sup>+</sup> T cells with [U-<sup>13</sup>C<sub>4</sub>]-βOHB and measured the enrichment of <sup>13</sup>C-labeled acetyl groups on histone H3 via mass spectrometry (Fig. 7G–H). Carbon from [U-<sup>13</sup>C<sub>4</sub>]-βOHB was enriched on histone H3K27 in control but not *Bdh1*<sup>-/-</sup> T cells (Fig. 7G), establishing ketolysis as an obligate step for βOHB-dependent

H3K27Ac in CD8<sup>+</sup> T cells. We also observed enrichment of [U-<sup>13</sup>C<sub>4</sub>]-βOHB carbon in acetyl groups from multiple lysine residues on histone H3 (K18, K23, K36, K115) and H4 (K5, K8, K12, K16) in control but not *Bdh1*<sup>-/-</sup> T cells (Fig. 7H). Next, we used quantitative chromatin immunoprecipitation coupled to next generation sequencing (ChIP-seq)<sup>50</sup> to assess the impact of *Bdh1* deficiency on H3K27Ac modifications in CD8<sup>+</sup> T cells at genome-scale resolution. Overall, we observed a global reduction of H3K27Ac in activated *Bdh1*<sup>-/-</sup> T cells compared to controls (Fig. S7B). Notably, we observed reduced H3K27Ac at the promoters of effector gene loci—including *Ifng*, *Gzmb*, *Prfl*, and *Tbx21* (Tbet)—in *Bdh1*<sup>-/-</sup> CD8<sup>+</sup> T cells, while H3K27Ac enrichment at loci associated with CD8<sup>+</sup> T cell identity and signal transduction (i.e., *Cd3e*, *Cd8a*, *Zap70*) were similar between control and *Bdh1*<sup>-/-</sup> T cells (Fig. 7I, S7B). In line with these observations, blocking CBP/p300 histone acetyltransferase (HAT) activity impaired IFN-γ production by CD8<sup>+</sup> T cells activated in the presence of βOHB (Fig 7J). This decrease in IFN-γ was also observed in *Bdh1*<sup>-/-</sup> T cells treated with the HAT inhibitor, which is consistent with the fact that other nutrients (i.e., glucose) can still contribute to the acetyl-CoA pool in *Bdh1*<sup>-/-</sup> cells (Fig. 6D) and highlights the importance of H3K27Ac for the stable expression of IFN-γ by CD8<sup>+</sup> T cells. Taken together, KB-dependent acetyl-CoA production supports CD8<sup>+</sup> T cell effector function, in part, by directly altering acetylation-dependent epigenetic programming at effector gene loci.

## Discussion

Physiologic KB concentrations are highly dynamic and influenced by circadian rhythm, diet, feeding behavior, and exercise<sup>26,27</sup>. In healthy adult humans and mice, the concentration of KBs in circulation is <1 mM (approx. 0.05–0.25 mM and 0.30–0.85 mM in humans and mice, respectively)<sup>26,27,32,38,51</sup>. During infection, disrupted feeding behavior, inflammation, and systemic metabolic rewiring promote changes in host metabolism, including the production of KBs as shown in this study and by others<sup>14–17,52</sup>. However, the impact that these host metabolic changes have on immunity, specifically CD8<sup>+</sup> T cell responses, remains poorly understood. Here, we identified cell-intrinsic ketolysis as a non-redundant metabolic feature of CD8<sup>+</sup> T cells that boosts effector function by altering T cell metabolism, and effector gene expression through effects on histone acetylation. Our data established KBs as potent bioenergetic substrates for CD8<sup>+</sup> T cells—preferred over glucose as a TCA cycle fuel—that increase mitochondrial respiratory capacity and TCA cycle-dependent biosynthesis *in vitro* and *in vivo*.

We found that the effects of βOHB on CD8<sup>+</sup> T cell bioenergetics were dependent on *Bdh1* expression, but not Scot. Unlike the biochemical reaction catalyzed by SCOT, the dehydrogenation of βOHB by *Bdh1* directly generates NADH. It is likely that Scot-depleted CD8<sup>+</sup> T cells still use βOHB to generate NADH, which can fuel ATP production despite incomplete oxidation of βOHB via ketolysis. In addition to effects on mitochondrial respiration, we showed that βOHB increased glycolysis and glycolytic ATP production in CD8<sup>+</sup> T cells. This result was unexpected, as βOHB has been reported to inhibit glucose uptake<sup>33,53</sup> and decrease glycolysis<sup>17,54,55</sup> in several other cell types. In CD8<sup>+</sup> T cells, glycolysis and ketolysis occur concomitantly<sup>32</sup>. We showed that βOHB availability reduced the fraction of TCA cycle carbon derived from glucose, which may spare glucose to support

glycolytic metabolism and the production of metabolites (i.e., nucleotides) required for T cell proliferation<sup>31,32,56</sup>. Taken together, our findings suggest that the dynamic relationship between glucose and KB metabolism may be cell type- and/or context-dependent and warrant further investigation.

A major point of this study was our demonstration that impairing  $\beta$ OHB oxidation by T cells compromised effector responses to bacterial or tumor challenge in mice fed a standard diet, establishing ketolysis as a physiologic regulator of T cell function. We speculate that ketolysis in CD8<sup>+</sup> T cells evolved as a metabolic program to preserve (and potentially boost) effector function during periods of starvation or disease-induced changes in feeding behavior<sup>57</sup>. Our findings raise the question whether manipulating systemic KB availability with dietary interventions (i.e., fasting, ketogenic diets) can be used as a strategy to augment CD8<sup>+</sup> T cell responses during infection and/or within tumors. Consistent with this idea, it was recently reported that CD8<sup>+</sup> T cells isolated from healthy individuals subjected to a ketogenic diet for 3 weeks display greater cytokine production and cytolytic activity *ex vivo*<sup>58</sup>.

KBs have been documented to impact several immune cell types, including macrophages<sup>59,60</sup>, neutrophils<sup>61</sup>, and T cells<sup>17,37,62–64</sup>, but most studies have focused on ketolysis-independent roles of KBs in immunity. Our results point towards ketolysis-driven acetyl-CoA synthesis as a mechanism underlying the immunomodulatory effects of  $\beta$ OHB on CD8<sup>+</sup> T cell function. We established that  $\beta$ OHB is a major source of acetyl-CoA production in Teff cells, which directly contributes to histone acetylation, and promotes permissive H3K27Ac at effector gene loci (i.e., *Ifng*, *Gzmb*, *Tbx21*). In contrast, previous work demonstrates that CD8<sup>+</sup> Tmem cells divert acetyl-CoA to synthesize  $\beta$ OHB, which supports the survival and maintenance of Tmem cells through histone  $\beta$ -hydroxybutyrylation<sup>37</sup>. Unlike CD8<sup>+</sup> Tmem cells, we found that Teff cells rely primarily on exogenous  $\beta$ OHB to fuel acetyl-CoA-dependent processes. Moreover, ketolysis-deficient CD8<sup>+</sup> T cells displayed no major defects in *Lm*-OVA-induced memory formation or recall responses. Interestingly, however, we observed an increased  $\beta$ OHB pool in *Bdh1*<sup>-/-</sup> cells, suggesting that inhibition of ketolysis may increase the availability of  $\beta$ OHB for ketolysis-independent processes, including  $\beta$ -hydroxybutyrylation. Collectively, these data suggest that  $\beta$ OHB may function via distinct immunomodulatory mechanisms in different CD8<sup>+</sup> T cell states.

Our immunophenotyping analysis suggested that CD8<sup>+</sup> T cell differentiation was not grossly affected when cell-intrinsic ketolysis was disrupted. The primary effect of disrupting ketolysis in Teff cells was impaired effector function, including reduced cytokine production and cytolytic activity. Transcriptionally, ketolysis-deficient Teff cells exhibited features consistent with early T cell exhaustion (Tex<sup>eff</sup> cells) and reduced cytotoxicity. In line with these data, we showed that tumor growth was accelerated in mice with *Bdh1*-deficient T cells. Future studies focused on the role of KB metabolism in the tumor microenvironment are warranted, especially given recent evidence demonstrating that ketogenic diets can potentiate the anti-cancer effects of PD-1 blockade<sup>65,66</sup>. Our data further highlight ketolysis as a potential target for advancing T cell-based immunotherapies, where increasing circulating concentrations of KBs may augment CD8<sup>+</sup> T cell function, especially when fuels

such as glucose are limiting. In summary, our data establish CD8<sup>+</sup> T cell-intrinsic ketolysis as a non-redundant, physiologic regulator of CD8<sup>+</sup> T cell function.

### Limitations of the study

Our *in vivo* studies focused on CD8<sup>+</sup> Teff cells in the context of physiologic KB concentrations in tumor-bearing or *Listeria*-infected mice fed a standard diet. We did not assess the impact of dietary interventions such as fasting or ketogenic diets on CD8<sup>+</sup> T cell effector function. Furthermore, all experiments were performed using mouse T cells, and therefore the extent to which our observations translate to human T cells remains to be elucidated. Finally, we did not explore whether the timing of  $\beta$ OHB availability (i.e., during priming versus after effector differentiation) influences its effects on T cell function. These experiments will be a focus of future studies.

## STAR Methods

### RESOURCE AVAILABILITY

**Lead Contact.**—Additional information and request for resources and reagents should be directed to and will be made available by the corresponding author, Russell G. Jones (russell.jones@vai.org).

**Materials Availability.**—All unique/stable reagents generated in this study will be made available from the Lead Contact with a completed Materials Transfer Agreement. Plasmids generated in this study will be deposited to Addgene.

**Data and Code Availability:** All data are available in the main text, supplemental figures/tables, or data repositories. The RNA-seq data used for the meta-analysis in Figure 1 are available at NCBI GEO (accession numbers (GSE86881, GSE89307, GSE84820)). The RNA-seq data from ketolysis-deficient CD8<sup>+</sup> T cells and H3K27Ac ChIP-seq data from *Bdhl*<sup>-/-</sup> CD8<sup>+</sup> T cells are available at NCBI GEO (accession: GSE229359). The mass spectrometry histone proteomics data were deposited to the ProteomeXchange Consortium via the PRIDE partner repository with the dataset identifier PXD036292. Bioenergetics data analysis was based on protocols developed by Mookerjee and Brand<sup>70</sup>, which is available for download at <https://russelljoneslab.vai.org/tools>.

### EXPERIMENTAL MODEL AND SUBJECT DETAILS

**Mice**—C57BL/6J, CD90.1 (Thy1.1<sup>+</sup>), B6.SJL-*Ptprca*<sup>a</sup> *Pepc*<sup>b</sup>/BoyJ (CD45.1<sup>+</sup>), Tg(TcraTcrb)1100Mjb (OT-I), and B6.Cg-Tg(Cd4-cre)1Cwi/BfluJ (*Cd4-Cre*) mice were purchased from The Jackson Laboratory. *Bdhl*-floxed animals were generated by Daniel Kelly<sup>33</sup>. *Oxct1*-floxed animals were generated by Peter Crawford<sup>51</sup>. Mice were bred and maintained under specific pathogen-free conditions at VAI under approved protocols. Genotyping was performed using DNA extracted from tail or ear biopsies and defined primer sets (see Table S5). Experiments were performed using female mice between 8 and 20 weeks of age.

**Cell lines**—293T (CRL-3216) and MC38-OVA (kindly provided by John Stagg) cells were cultured in Dulbecco's Modified Eagle's Medium (DMEM) (Wisent Inc., St. Bruno, QC, Canada) supplemented with 10% heat-inactivated fetal bovine serum (FBS), 1% penicillin-streptomycin (Gibco), and L-glutamine at a final concentration of 6 mM. 293T and MC38-OVA cells are female. All cells were cultured at 37°C in a humidified 5% CO<sub>2</sub> incubator.

## METHOD DETAILS

**T cell purification and culture**—For mouse T cell isolations, total or CD8<sup>+</sup> T cells were purified from spleen and peripheral lymph nodes by negative selection (StemCell Technologies, Vancouver, BC, Canada). Purified CD8<sup>+</sup> T cells were used for all experiments except the *in vitro* T cell activation and cytokine production assays, where total T cells were purified and the CD8<sup>+</sup> T cell subset was analyzed. Cells were cultured in Iscove's Modified Delbecco's Medium (IMDM) or Van Andel Institute-modified Iscove's Medium (VIM)<sup>32</sup> supplemented with 1% penicillin-streptomycin (Gibco) and 50 μM of 2-mercaptoethanol (2-ME; Gibco). For standard T cell cultures, IMDM was supplemented with 10% Nu-Serum IV culture supplement (Corning). VIM was supplemented with 10% dialyzed FBS (Corning). Unless stated otherwise, CD8<sup>+</sup> T effector (Teff) cells were generated by activation in standard IMDM containing 25 mM glucose and 6 mM L-glutamine. For physiologic culture conditions, Seahorse experiments, and <sup>13</sup>C tracing experiments, CD8<sup>+</sup> Teff cells were culture in medium containing 5 mM glucose and 0.5 mM L-glutamine. Physiologic carbon sources (PCS) were added to culture media (IMDM or VIM) as indicated at the following concentrations: acetate (400 μM), βOHB (850 μM), citrate (215 μM), lactate (3 mM), and pyruvate (150 μM)<sup>32</sup>. *In vitro*-activated CD8<sup>+</sup> Teff cells were generated by stimulating naïve CD8<sup>+</sup> T cells (1 × 10<sup>6</sup> cells/mL) with plate-bound anti-CD3ε (clone 145-2C11; 2 μg/mL) and anti-CD28 (clone 37.51; 1 μg/mL) antibodies (eBioscience, San Diego, CA) for 2–3 days. For extracellular flux analysis, stable isotope labeling, and histone isolation procedures, activated CD8<sup>+</sup> Teff cells were re-cultured (2–5 × 10<sup>6</sup> cells/well in 6-well plates) for up to 48 h in IMDM containing 50 U/mL IL-2 (PeproTech, Rocky Hill, NJ) prior to use in assays. For retroviral transduction experiments, CD8<sup>+</sup> Thy1.1<sup>+</sup> OT-I T cells (control or *Bdh1*<sup>-/-</sup>) were transduced with retrovirus 24 h post-activation and expanded for 2 additional days in IMDM containing IL-2 as previously described<sup>31,32</sup>. Transduced T cells were sorted by fluorescence-activated cell sorting (FACS) and cultured overnight prior to adoptive transfer into sex-matched naïve Thy1.2<sup>+</sup> C57BL/6J hosts.

**Adoptive transfer and infection with *L. monocytogenes* (*Lm-OVA*)**—Mice were immunized intravenously with a sublethal dose of recombinant attenuated *Listeria monocytogenes* expressing OVA (*Lm-OVA*, 2 × 10<sup>6</sup> CFU) as previously described<sup>10,56</sup>. For adoptive transfer experiments 6–7 days post-infection (dpi) using non-transduced or transduced cells, 5 × 10<sup>3</sup> OT-I CD8<sup>+</sup> T cells (Thy1.1<sup>+</sup> or CD45.2<sup>+</sup>) were injected intravenously into C57BL/6J mice (Thy1.2<sup>+</sup>CD45.2<sup>+</sup> or CD45.1<sup>+</sup>), followed by *Lm-OVA* infection 1 day later. Splenocytes were isolated from mice 7 dpi and analyzed for the presence of OVA-specific CD8<sup>+</sup> T cells by Thy1.1 or CD45.2 staining and cytokine production analyzed by intracellular cytokine staining (ICS) following peptide re-stimulation (OVA<sub>257-264</sub>) as previously described<sup>10,56</sup>. For *ex vivo* <sup>13</sup>C tracing, Thy1.2<sup>+</sup>CD45.2<sup>+</sup> C57BL/6J mice received 5 × 10<sup>4</sup> Thy1.1<sup>+</sup> OT-I CD8<sup>+</sup> T cells intravenously

and were infected with *Lm*-OVA 1 day later. Activated Thy1.1<sup>+</sup> OT-I T cells were isolated from the spleen 7 dpi by magnetic bead isolation for Thy1.1 as previously described<sup>31,43</sup>, followed by short-term (2 h) cell culture *in vitro* in VIM containing 0–2 mM  $\beta$ OHB. For metabolic analysis of *Lm*-OVA-specific Thy1.1<sup>+</sup> OT-I T cells *in vivo* using <sup>13</sup>C-labeled metabolites, Thy1.2<sup>+</sup>CD45.2<sup>+</sup> C57BL/6J mice received  $2.5 \times 10^6$  or  $5 \times 10^4$  Thy1.1<sup>+</sup> OT-I CD8<sup>+</sup> T cells for analysis at 2 and 6 dpi, respectively. *Lm*-OVA-specific OT-I CD8<sup>+</sup> T cells were isolated from the spleen of infected mice by positive selection using the EasySep mouse CD90.1 (Thy1.1) positive selection kit (StemCell Technologies) as previously described<sup>31,43</sup>.

For memory rechallenge experiments, mice were immunized intravenously with a sublethal dose ( $2 \times 10^6$  CFU) of attenuated *Lm*-OVA, followed by rechallenge with a lethal dose of recombinant virulent *Lm*-OVA ( $1 \times 10^6$  CFU) 45 days after primary immunization. Splenocytes were isolated 5 days post-rechallenge and analyzed as described above.

**Retrovirus and lentivirus production**—For retrovirus production, 293T cells were co-transfected with pCL-Eco and either pLMPd-Amt shFF (control vector) or sh*Oxct1* using Lipofectamine 2000 transfection reagent (Invitrogen) according to the manufacturer's protocol. Viral supernatants were harvested 48 and 72 h post-transfection, pooled, and concentrated using Lenti-X Concentrator (Takara Bio) according to the manufacturer's protocol. The concentrated retrovirus was added to 24 h-activated T cells together with 8 ng/mL polybrene, 200 U/mL IL-2, and 20 mM HEPES, and the cells were centrifuged at 1180 RCF, 30°C for 90 min. Ametrine-positive cells were sorted by FACS 48–72 h post-transduction. For lentivirus production, 293T cells were co-transfected with pLentiviral-S-tdTomato, pCMV-VSV-G, and pSPAX2 using FuGENE 6 transfection reagent (Promega) according to the manufacturer's protocol. The lentiviral supernatant was harvested 48 h post-transfection and MC38-OVA cells were transduced with the virus + 8  $\mu$ g/mL polybrene. TdTomato-expressing MC38-OVA cells were sorted 48 h post-transduction.

**T cell killing assay**—CD8<sup>+</sup> T cells were purified from the spleens of *Bdh1<sup>fl/fl</sup>OT-I<sup>Tg/+</sup>* or *Bdh1<sup>fl/fl</sup>OT-I<sup>Tg/+</sup>Cd4-Cre* mice as described above, activated in standard IMDM for 2 days with 1  $\mu$ g/mL OVA257–264 peptide in the presence of 5 mM  $\beta$ OHB, and expanded for an additional 2 days in 5 mM  $\beta$ OHB + 5 U/mL IL-2. TdTomato-expressing MC38-OVA cells were seeded in a 96-well plate ( $5 \times 10^3$  cells/well). 24 h later, a range of  $3 \times 10^5$  to 586 activated OT-I CD8<sup>+</sup> T cells (control or *Bdh1<sup>-/-</sup>*) were added to the MC38-OVA tumor cells in standard IMDM supplemented with 5 mM  $\beta$ OHB and 5 U/mL IL-2. TdTomato<sup>+</sup> cells were quantified over a 24 h period using IncuCyte live-cell analysis (Sartorius). The percentage of dead MC38-OVA tumor cells was calculated by normalizing the number of TdTomato-expressing cells to media-only (no T cell) controls.

**MC38-OVA tumor model**—9–11-week-old female *Bdh1<sup>fl/fl</sup>Cd4-Cre* mice or *Bdh1<sup>fl/fl</sup>* control littermates were injected with  $5 \times 10^5$  MC38-OVA cells subcutaneously in the abdominal flank. Once palpable tumors were present, tumor measurements were obtained every 2–3 days using a caliper. Mice were euthanized as they reached humane endpoints, which included a maximum tumor volume of 1500 mm<sup>3</sup>.

**Flow cytometry**—Single cell suspensions from the spleen were stained with a cocktail of fluorescently-labeled antibodies listed in the Key Resources Table. Cell viability was assessed by using Fixable Viability Dye (FVD) eFluor 506 or FVD eFluor 780 according to the manufacturer's protocols. Cell proliferation was assessed by Violet Proliferation Dye 450 (VPD450) dilution according to the manufacturer's protocol. To assess cytokine production, splenocytes were plated in the presence of PMA (50 ng/mL) and ionomycin (50 ng/mL) for 4 h, with GolgiStop (1:1500 dilution) added for the last 2 h of stimulation prior staining. After restimulation, cells were stained with surface marker antibodies, fixed and permeabilized using the FoxP3/Transcription Factor Staining Buffer Set, and then stained with intracellular marker antibodies. For analysis of antigen-specific responses to *Lm*-OVA, splenocytes harvested 7 dpi were stimulated with OVA257<sub>264</sub> peptide using previously published protocols<sup>31</sup>. Analytical flow cytometry was performed on CytoFLEX (Beckman Coulter) or Cytex Aurora cytometers and cell sorting on Astrios (Beckman Coulter) or BD FACSAria Fusion cell sorters. Data analysis was performed using FlowJo software (Tree Star).

**Extracellular flux analysis**—T cell oxygen consumption rate (OCR) and extracellular acidification rate (ECAR) were measured using a Seahorse XF96 Extracellular Flux Analyzer following established protocols<sup>31</sup>. Activated and IL-2-expanded T cells ( $1.5 \times 10^5$ /well) were cultured in XF medium containing 5 mM glucose, 0.5 mM glutamine, and 2 mM sodium pyruvate following centrifugation onto poly-D-lysine-coated XF96 plates, and cellular bioenergetics assessed at 5 minute intervals following the sequential addition of oligomycin (2  $\mu$ M), fluoro-carbonyl cyanide phenylhydrazone (FCCP, 1.5  $\mu$ M), rotenone/antimycin A (0.5  $\mu$ M each), and monensin (20  $\mu$ M). Data were normalized to cell number. Where indicated,  $\beta$ OHB (2 mM) or AcAc (2 mM) were added to cell culture for 2 h prior to Seahorse analysis and added to Seahorse medium over the assay period. Bioenergetics data analysis was based on protocols developed by Mookerjee and Brand<sup>70</sup>, which is available for download at <https://russelljoneslab.vai.org/tools>.

**Acetoacetate synthesis**—For *in vitro* assays involving acetoacetate, [<sup>12</sup>C<sub>4</sub>]-ethyl acetoacetate (Sigma-Aldrich) and [<sup>13</sup>C<sub>4</sub>]-ethyl-acetoacetate (Cambridge Isotope Laboratories) were hydrolyzed by mixing 1 mL of ethyl acetoacetate with 8 mL of 1 M NaOH at 60°C by stirring for 30 min. Hydrolyzed samples were placed on ice and adjusted to pH 7.5 using 50% HCl. Metabolite aliquots were subsequently frozen and stored at -80°C. The concentration of synthesized acetoacetate was evaluated using the Autokit Total Ketone Bodies Assay (Fujifilm Wako).

**Stable isotope labeling (SIL) and metabolomics**—SIL experiments with *in vitro*-activated T cells using liquid chromatography (LC) or gas chromatography (GC) coupled to mass spectrometry (MS) were conducted as previously described<sup>31,32,43</sup>. In brief, naïve CD8<sup>+</sup> T cells were activated as above, washed with IMDM or VIM containing 10% dialyzed FBS, and re-cultured ( $2.5 \times 10^6$  cells/well in 24-well plates) for indicated times in medium containing <sup>13</sup>C-labeled metabolites at the following concentrations: [U-<sup>13</sup>C<sub>6</sub>]-glucose, 5 mM; [U-<sup>13</sup>C<sub>2</sub>]-acetate, 400  $\mu$ M; [U-<sup>13</sup>C<sub>4</sub>]-AcAc, 2 mM; [U-<sup>13</sup>C<sub>3</sub>]-alanine, 200  $\mu$ M; [U-<sup>13</sup>C<sub>4</sub>]- $\beta$ OHB, 0.85 or 2 mM; [U-<sup>13</sup>C<sub>6</sub>]-citrate, 215  $\mu$ M; [U-<sup>13</sup>C<sub>3</sub>]-lactate, 3 mM;

[U-<sup>13</sup>C<sub>3</sub>]-pyruvate, 150 μM. Cells were transferred from tissue culture plates to conical tubes and centrifuged at 500 RCF, 4°C for 3 min. The cell pellet was washed with ice-cold saline before being snap frozen on dry ice and stored at -80°C. Metabolites were extracted as described previously<sup>32</sup>.

For acetyl-CoA measurements, metabolite extracts were resuspended in 100% water and analyzed by LC-MS. The LC column was CORTECS T3 Column, 120 Å, 1.6 μm, 2.1 mm × 150 mm (Waters, #186008500) with a CORTECS T3 VanGuard Pre-column, 120 Å, 1.6 μm, 2.1 mm × 5 mm (Waters, #186008508). Mobile phase A was 100% water and mobile phase B was 99% acetonitrile (v/v). Both mobile phases contained 5 mM ammonium acetate and 0.01% ammonium hydroxide (v/v). The LC flow rate was 300 μL/min and the gradient was as follows: 0 – 0.5 min, 0% B; 0.5 – 1.0 min, ramp to 10% B; 1.0 – 7.5 min, ramp to 100% B; 7.5 – 10.0 min, hold at 100% B. The column was re-equilibrated at 100% A for 10 min. The mass spectrometer was an Orbitrap ID-X (Thermo) operated in ESI-positive mode with targeted select ion monitoring (tSIM) for acetyl-CoA ( $m/z = 810.1131 \pm 20$  m/z) between retention time 1 – 4 min with an expected retention time of 2.7 min. Source conditions were as reported previously<sup>32</sup>.

For βOHB quantitation in serum, liver, and spleen, metabolites were extracted with ice cold 40% acetonitrile, 40% methanol, and 20% water (v/v). An external standard curve for βOHB was prepared from 10 μg/mL to 0.01 μg/mL by half-log serial dilutions. Standards were extracted and handled identically to tissue/serum throughout the workflow. Tissues were extracted at a concentration of 40 mg tissue/mL of extraction solvent and serum at 40 μL serum/mL of extraction solvent. Extracts were dried and resuspended in water (200 μL for tissue, 1 mL for serum) containing 100 ng/mL of internal standard ([U-<sup>13</sup>C<sub>4</sub>]-βOHB). Samples and standards were analyzed on an Orbitrap Exploris 240 (Thermo) in ESI-negative mode using a tributylamine ion-paired chromatography as described previously<sup>32</sup>. Data were analyzed in Skyline and internal standard normalized peak areas from samples and standards were used to calculate βOHB concentrations. Calculated sample concentrations in μg/mL were transformed to mg/g tissue or mM for serum.

***In vivo* <sup>13</sup>C tracer infusions**—*In vivo* infusions of *Lm*-OVA-infected mice were conducted using previously described protocols<sup>31,43</sup>. Briefly, mice were anesthetized using isoflurane and infused intravenously with <sup>13</sup>C-labeled tracers over a 2 h period. [U-<sup>13</sup>C<sub>6</sub>]-glucose infusions were performed as previously described, using a stock concentration of 100 mg/mL, an initial bolus dose of 120 μL and infusion rate of 2.5 μL/min for 2 h for a 20 g mouse. For infusions of sodium D-[U-<sup>13</sup>C<sub>4</sub>]-βOHB, mice received an initial bolus of 0.487 mg per gram of mouse, followed by infusion of 0.05 μL/min/g bodyweight using a 1.5 M stock concentration for 2 h. Subsequently, mice were cervically dislocated, blood was harvested via cardiac puncture, centrifuged at 500 RCF, 4°C for 3 min, and serum was snap frozen in liquid nitrogen. Spleens were collected and processed for Thy1.1<sup>+</sup> T cell isolation by magnetic bead isolation. Isolated T cells were snap frozen on dry ice and subsequently processed for metabolomic analysis as described.

**RNA isolation, sequencing, and qPCR analysis**—Total RNA was isolated from murine T cells via RNeasy Kit (Qiagen) with DNase digestion (Qiagen) following the

manufacturers' instructions. For quantitative PCR (qPCR) analysis, total RNA was reverse transcribed using a High-Capacity cDNA Reverse Transcriptase kit (Life Technologies) and qPCR performed using universal SYBR green supermix (Bio-Rad). Results were normalized to *Stk11* mRNA expression and control conditions using standard ddCt methods. RNA preparation and library construction for RNA-seq was conducted by the VAI Genomics Core as previously described<sup>71</sup>. Libraries were sequenced using a NovaSeq 6000 (Illumina) using 50 bp paired-end sequencing ( $5 \times 10^7$  reads/sample). Gene-set enrichment analysis (GSEA) of RNA-seq data was conducted using the gage function and non-parametric Kolmogorov–Smirnov test from the GAGE (version 2.22.0) R Bioconductor package<sup>72</sup>. RNA-seq data files are available at NCBI GEO (accession: GSE212048).

For the meta-analysis in Figure 1, raw sequences from RNA-seq of CD8<sup>+</sup> T cells from three previously published studies (GEO accessions: GSE89307, GSE84820, and GSE86881) were downloaded. Adaptor sequences and low-quality reads were trimmed using Trim Galore (v0.6.0). Trimmed reads were aligned to the mm10 reference genome using STAR (v2.7.8)<sup>73</sup>. Count tables of all samples were then imported into limma (v3.48.3)<sup>74</sup>, with a batch variable included in the design matrix to account for the different study designs and sequencing platforms. Pearson correlations among samples were calculated using batch corrected, variance stabilization transformed counts using DESeq2 (v1.32)<sup>75</sup>, and the Pearson correlation matrix was used to generate a heatmap. Batch corrected counts were also used to conduct principal component analysis (PCA) using DESeq2. Differential gene expression analyses of two main comparisons (comparison 1: cancer Tex cells vs. Teff cells; comparison 2: virus Tex cells vs. Teff cells) were conducted on raw counts using DESeq2, with a covariate to adjust for batch, and Benjamini-Hochberg adjusted p-values to maintain a 5% false discovery rate. The median of the two Wald test statistics for each gene, one from each of the two comparisons, were used for gene rankings. Gene ontology (GO) terms for each gene was retrieved from BioMart using R package biomaRt (v2.48.4)<sup>76,77</sup>. Lastly, for each comparison, genes were sorted by their fold change from highest to lowest (using Teff cells as reference in both comparisons) and GSEA<sup>78</sup> was conducted for each comparison independently using clusterProfiler (v4.0.5)<sup>79</sup>. Gene sets C2, C5, C6, C7, and Hallmark for mm10 was retrieved from Molecular Signatures Database using R package MSigDB (7.4.1).

**Immunoblotting**—Cells were lysed in RIPA or modified Laemmli lysis buffer (240 mM Tris/HCl pH 6.8, 40% glycerol, 8% SDS, 5% 2-ME) supplemented with protease and phosphatase inhibitor cocktails (Roche). A Pierce BCA Protein Assay Kit (Thermo Fisher Scientific, Waltham, MA, USA) was used to quantify protein from whole cell lysates. Equal amounts of protein were diluted in Laemmli sample buffer, boiled for 5 min, and resolved by SDS-PAGE on a 10% gel. Proteins were transferred onto PVDF or nitrocellulose membranes. Membranes were blocked for 1 h in 5% non-fat milk in TBST at room temperature and incubated with primary antibodies against *Bdh1*, Scot (Oxct1),  $\beta$ -tubulin, or  $\beta$ -actin overnight at 4°C. Membranes were washed three times for 5 min with 1x TBST, and then incubated for 1 h at room temperature with the corresponding secondary HRP-conjugated antibody diluted in 5% non-fat milk. Membranes were washed three times with 1x TBST and then developed using ECL solution (Cytiva). Histone proteins were extracted from T cells using a Histone Extraction Kit (Abcam) following the

manufacturer's instructions. Lysates containing 0.5–2 µg of protein were resolved on a 4–20% SDS-PAGE gel and transferred to PVDF membrane. Membranes were incubated with primary and secondary antibodies and developed with ECL solution as described above. Primary antibodies are listed in the Key Resources Table.

**Proteomic analysis**—For proteomic analysis of histones, activated CD8<sup>+</sup> T cells were cultured in VIM (5 mM glucose, 0.5 mM glutamine) containing 5 mM [<sup>12</sup>C<sub>4</sub>]-βOHB or [<sup>13</sup>C<sub>4</sub>]-βOHB for 24 h. Histone isolation was carried out using the same methodology for immunoblotting, with the addition of 2 ice-cold PBS washes. Histone extracts were lyophilized and resuspended in 50 µL of 8 M urea with 10 mM HEPES-KOH pH 7.5. Proteins were reduced by adding dithiothreitol (DTT) to a final concentration of 5 mM and by heating at 95°C for 2 min, followed by a 30 min incubation at room temperature. The alkylation of the proteins was carried out by adding chloroacetamide (Sigma-Aldrich) to a final concentration of 7.5 mM, followed by a 20 min incubation in the dark at room temperature. The urea concentration was then diluted to a final concentration of 2 M by adding 150 µL of 50 mM ammonium bicarbonate (NH<sub>4</sub>HCO<sub>3</sub>) (Sigma-Aldrich). Digestion was started by adding 1 µg of Pierce MS-grade trypsin (Thermo Fisher Scientific) and samples were incubated overnight at 30°C with shaking. Samples were then acidified by adding trifluoroacetic acid (TFA) (Sigma-Aldrich) to a final concentration of 0.2%.

The peptides were purified with ZipTip 100-µL micropipette tips containing a C18 column, according to the manufacturer's protocol (EMD Millipore, Burlington, VT) and eluted with 300 µL of 50% ACN/1% FA buffer in an additional low-binding microtube. The peptides were then concentrated by centrifugal evaporator at 60°C until complete drying (~3 h) and then resuspended in 50 µL of 1% FA buffer. Peptides were assayed using a NanoDrop spectrophotometer (Thermo Fisher Scientific, Waltham, MA) and read at an absorbance of 205 nm. The peptides were then transferred to a glass vial (Thermo Fisher Scientific) and stored at –20°C until analysis by mass spectrometry.

For LC-MS analysis, 250 ng of peptides were injected into an HPLC (nanoElute, Bruker Daltonics) and loaded onto a trap column (Acclaim PepMap100 C18 column, 0.3 mm id × 5 mm, Dionex Corporation) with a constant flow of 4 µL/min, then eluted onto an analytical C18 Column (1.9 µm beads size, 75 µm × 25 cm, PepSep). Peptides were eluted over a 2-h gradient of ACN (5–37%) in 0.1% FA at 400 nL/min while being injected into a TimsTOF Pro ion mobility mass spectrometer equipped with a Captive Spray nano electrospray source (Bruker Daltonics). Data were acquired using data-dependent auto-MS/MS with a 100–1700 m/z mass range, with PASEF enabled with several PASEF scans set at 10 (1.17 seconds duty cycle) and a dynamic exclusion of 0.4 min, m/z dependent isolation window and collision energy of 42.0 eV. The target intensity was set to 20,000, with an intensity threshold of 2,500.

Raw data files were analyzed using MaxQuant (v2.0.3.0) and the Uniprot human proteome database (21/03/2020, 75,776 entries). The settings used for the MaxQuant analysis (with TIMS-DDA type in group-specific parameters) were: 4 miscleavages were allowed; the minimum peptide length was set to 5; enzyme was Trypsin (K/R not before P); fixed modification was carbamidomethylation on cysteine; variable modifications were

methionine oxidation, protein N-terminal acetylation ( $^{12}\text{C}$ ,  $^{13}\text{C}$ ), lysine (K) acetylation ( $^{12}\text{C}$ ,  $^{13}\text{C}$ ), and protein carbamylation (K, N-terminal). A mass tolerance of 20 ppm was used for both precursor and fragment ions. Identification values “PSM FDR”, “Protein FDR”, and “Site decoy fraction” were set to 0.05. Minimum peptide count was set to 1. Both the “Second peptides” and “Match between runs” options were also allowed. Compass DataAnalysis (v5.3, Bruker Daltonics) was further used to represent both spectral and graphical MS<sup>1</sup> results for specific peptides.

Proteomic analysis of *in vivo*-activated OT-I CD8<sup>+</sup> Teff cells isolated 6 dpi with attenuated *Lm*-OVA was performed as previously described<sup>31</sup>, with matched data from 2.5 dpi published previously<sup>31</sup>.

**Chromatin immunoprecipitation sequencing (ChIP-seq) analysis**—ChIP-seq analysis of H3K27Ac enrichment in CD8<sup>+</sup> T cells was conducted using the sans spike-in quantitative ChIP (siQ-ChIP) method as previously described<sup>50,80</sup>. Naïve CD8<sup>+</sup> T cells ( $5 \times 10^6$ ) were activated with anti-CD3 and anti-CD28 antibodies for 24 h, then rinsed once with 10 mL of D-PBS (Gibco, 14190136) followed by cross-linking in suspension for 5 min in 10 mL of 0.75% formaldehyde (Pierce, 28906) in D-PBS at room temperature. Prior to every liquid removal step, cells were centrifuged at 800 RCF for 3 min. Formaldehyde was removed, and cells were quenched for 5 min with 10 mL of 750 mM Tris pH 10–10.5. Cells were washed twice with 10 mL of D-PBS, snap frozen in liquid nitrogen, and stored at  $-80^\circ\text{C}$ . Cells were then lysed under hypotonic conditions (1 mL of 20 mM Tris-HCl pH 8, 85 mM KCl, 0.5% NP-40 (1 tablet of protease inhibitor (Roche, 11836170001) per 5 mL of buffer)) for 30 min on ice. Nuclei were collected by centrifugation at 1300 RCF for 5 min, lysed by resuspension in nuclei lysis buffer (150  $\mu\text{L}$  50 mM Tris-HCl pH 8, 150 mM NaCl, 2 mM EDTA, 1% NP-40, 0.5% sodium deoxycholate, 0.1% SDS (1 tablet of protease inhibitor per 5 mL of buffer)), and passed through a 27-gauge needle (BD #309623, Lot: 0227218). Lysates were diluted to 500  $\mu\text{L}$  by addition of binding buffer (25 mM HEPES pH 7.5, 100 mM NaCl, 0.1% NP-40). 5  $\mu\text{L}$  of RNase A/T1 (Thermo Scientific, EN0551) was added, and the sample was incubated at  $37^\circ\text{C}$  for 25 min. Next,  $\text{CaCl}_2$  was added to a final concentration of 40 mM, followed by the addition of 75 U of micrococcal nuclease (Worthington Biochemical) and incubated at  $37^\circ\text{C}$  for 5 min. MNase was quenched by the addition of 40 mM EDTA, and the total volume was brought to 1.2 mL with binding buffer. Next, insolubilities were removed by centrifugation at max speed (about 21,000 RCF) at  $4^\circ\text{C}$  for 5 min, and the supernatant containing soluble chromatin was collected. At this stage, 5  $\mu\text{L}$  of chromatin was measured using the Qubit dsDNA HS Assay Kit (Invitrogen, Q32851).

Samples were diluted with binding buffer to ensure similar chromatin concentrations and to match IP conditions. 50  $\mu\text{L}$  of chromatin was set aside as input for each sample. For each IP, 25  $\mu\text{L}$  of Protein A-coated magnetic beads (Invitrogen, 10008D) were washed once with binding buffer and incubated with either 0, 2.5, or 10  $\mu\text{L}$  of H3K27Ac antibody (Active Motif #39133, lot: 16119013). Total volume of bead plus antibody was brought to 200  $\mu\text{L}$  using binding buffer and were rotated at room temperature for 30 min. For comparison of post-translational modifications between samples, we performed one biological replicate of all samples on the same day and made a master mix of bead plus antibody, scaling up all components by the number of samples. For example, for 2 samples with technical replicate

points, bead and antibody amounts were scaled by  $\times 4.2$  to account for dead volume. Buffer containing antibody was removed, and bead plus antibody were resuspended in 200  $\mu\text{L}$  of soluble chromatin followed by 30 min rotation at room temperature. Unbound chromatin was removed, and beads were vortexed for 10 s with 500  $\mu\text{L}$  of binding buffer. Buffer was removed, and bound material was eluted from beads by vortexing for 10 s in 133  $\mu\text{L}$  of elution buffer (25 mM HEPES pH 7.5, 100 mM NaCl, 1% SDS, and 0.1% NP-40). At this time, the input was brought to 133  $\mu\text{L}$  by the addition of 83  $\mu\text{L}$  elution buffer. Proteinase K (Invitrogen, 25530015) was added to a final concentration of 15  $\mu\text{M}$  and the sample was incubated overnight at 37°C. The following morning, each DNA sample was purified using MinElute PCR Kit (Qiagen, 28004) and eluted in 30  $\mu\text{L}$  of Buffer EB. 5  $\mu\text{L}$  of DNA was quantified by Qubit dsDNA HS Assay Kit. The remaining 25  $\mu\text{L}$  of DNA was frozen at  $-20^\circ\text{C}$  until library preparation.

Libraries were sequenced using a NextSeq 500 (Illumina) using 75 bp paired-end sequencing ( $5 \times 10^7$  reads/sample for IPs,  $1 \times 10^8$  reads/sample for input). Next generation sequencing (NGS) data were aligned to the mm10 genome. Bed files generated by the NGS alignment were processed using the latest siQ-ChIP release (found at <https://github.com/BradleyDickson/siQ-ChIP>) and siQ-ChIP quantification performed as previously described<sup>50</sup>. Responses were computed automatically by the siQ-ChIP software as the ratio of area under overlapping peaks for any pair of tracks being compared. Individual ChIP tracks were visualized using IGV<sup>81</sup>. Input files for siQ-ChIP and resulting output files and gnuplot script for plotting are available at NCBI GEO (accession: GSE229358).

**Quantification and statistical analysis**—Unless otherwise stated, data are presented as mean  $\pm$  standard deviation (SD) for technical replicates and mean  $\pm$  standard error of the mean (SEM) for biological replicates. Observations from technical replicate data were reproduced in at least two independent experiments. Statistical analyses were performed using GraphPad Prism software (GraphPad). A two-tailed, unpaired Student's t-test was used to compare the means between two independent groups. All other statistical tests are specified in the corresponding figure legends. Statistical significance is indicated in all figures by the following annotations: \*,  $p < 0.05$ ; \*\*,  $p < 0.01$ ; \*\*\*,  $p < 0.001$ ; \*\*\*\*,  $p < 0.0001$ ; ns, not significant.

## Supplementary Material

Refer to Web version on PubMed Central for supplementary material.

## Acknowledgements

### General:

We acknowledge Drs. Ralph DeBerardinis, Julian Lum, Sara Nowinski, Evan Lien, and members of the Jones and Krawczyk laboratories for scientific discussions contributing to this manuscript. We thank Teresa Leone, Matthew Vos, Jeanie Wedberg, Margene Brewer, and Michelle Minard for administrative assistance. We thank members of the Van Andel Institute (VAI) Core Facilities (Metabolomics and Bioenergetics, Genomics, Bioinformatics and Biostatistics, Flow Cytometry, Vivarium) for technical assistance.

**Funding:**

JL is supported by a VAI Metabolism & Nutrition (MeNu) Program Pathway-to-Independence Award and Canadian Institutes of Health Research (CIHR) Fellowship (MFE-181903). MJW is supported by a National Cancer Institute (NCI) T32 training grant (T32CA251066-01A1). DPK is supported by the National Institutes of Health (NIH, R01HL128349 and R01HL151345). CMK is supported by the National Institute of Allergy and Infectious Diseases (NIAID, R21AI153997) and VAI. FMB is a FRQS Senior Scholar (281824) and is supported by the National Sciences and Engineering Research Council of Canada (RGPIN-2018-05414). SBR is supported by the National Institute of General Medical Sciences (NIGMS, R35GM124736) and VAI. PAC and PP are supported by the National Institute of Diabetes and Digestive and Kidney Diseases (NIDDK, DK091538) and National Institute on Aging (NIA, AG069781). RGJ is supported by the Paul G. Allen Frontiers Group Distinguished Investigator Program, NIAID (R01AI165722), and VAI.

**Inclusion and Diversity**

We support inclusive, diverse, and equitable conduct of research.

**References**

1. Williams MA, and Bevan MJ (2007). Effector and memory CTL differentiation. *Annu. Rev. Immunol.* 25, 171–192. [PubMed: 17129182]
2. Philip M, and Schietinger A (2022). CD8+ T cell differentiation and dysfunction in cancer. *Nat. Rev. Immunol.* 22, 209–223. [PubMed: 34253904]
3. Pearce EL, Poffenberger MC, Chang C-H, and Jones RG (2013). Fueling immunity: insights into metabolism and lymphocyte function. *Science* 342, 1242454. [PubMed: 24115444]
4. O'Neill LAJ, Kishton RJ, and Rathmell J (2016). A guide to immunometabolism for immunologists. *Nat. Rev. Immunol.* 16, 553–565. [PubMed: 27396447]
5. Chapman NM, and Chi H (2022). Metabolic adaptation of lymphocytes in immunity and disease. *Immunity* 55, 14–30. [PubMed: 35021054]
6. Buck MD, Sowell RT, Kaech SM, and Pearce EL (2017). Metabolic Instruction of Immunity. *Cell* 169, 570–586. [PubMed: 28475890]
7. MacIver NJ, and Rathmell JC (2017). Editorial overview: Metabolism of T cells: integrating nutrients, signals, and cell fate. *Curr. Opin. Immunol.* 46, viii–xi. [PubMed: 28684058]
8. Cham CM, Driessens G, O'Keefe JP, and Gajewski TF (2008). Glucose deprivation inhibits multiple key gene expression events and effector functions in CD8+ T cells. *Eur. J. Immunol.* 38, 2438–2450. [PubMed: 18792400]
9. Chang C-H, Curtis JD, Maggi LB Jr, Faubert B, Villarino AV, O'Sullivan D, Huang SC-C, van der Windt GJW, Blagih J, Qiu J, et al. (2013). Posttranscriptional control of T cell effector function by aerobic glycolysis. *Cell* 153, 1239–1251. [PubMed: 23746840]
10. Blagih J, Coulombe F, Vincent EE, Dupuy F, Galicia-Vázquez G, Yurchenko E, Raissi TC, van der Windt GJW, Viollet B, Pearce EL, et al. (2015). The energy sensor AMPK regulates T cell metabolic adaptation and effector responses in vivo. *Immunity* 42, 41–54. [PubMed: 25607458]
11. Klein Geltink RI, Edwards-Hicks J, Apostolova P, O'Sullivan D, Sanin DE, Patterson AE, Puleston DJ, Lighthart NAM, Buescher JM, Grzes KM, et al. (2020). Metabolic conditioning of CD8+ effector T cells for adoptive cell therapy. *Nat Metab* 2, 703–716. [PubMed: 32747793]
12. Ayres JS (2020). Immunometabolism of infections. *Nat. Rev. Immunol.* 20, 79–80. [PubMed: 31892735]
13. Wilhelm C, Surendar J, and Karagiannis F (2021). Enemy or ally? Fasting as an essential regulator of immune responses. *Trends Immunol.* 42, 389–400. [PubMed: 33865714]
14. Wang A, Huen SC, Luan HH, Yu S, Zhang C, Gallezot J-D, Booth CJ, and Medzhitov R (2016). Opposing Effects of Fasting Metabolism on Tissue Tolerance in Bacterial and Viral Inflammation. *Cell* 166, 1512–1525.e12. [PubMed: 27610573]
15. Baazim H, Schweiger M, Moschinger M, Xu H, Scherer T, Popa A, Gallage S, Ali A, Khamina K, Kosack L, et al. (2019). CD8+ T cells induce cachexia during chronic viral infection. *Nat. Immunol.* 20, 701–710. [PubMed: 31110314]

16. Lercher A, Bhattacharya A, Popa AM, Caldera M, Schlapansky MF, Baazim H, Agerer B, Gürtl B, Kosack L, Májek P, et al. (2019). Type I Interferon Signaling Disrupts the Hepatic Urea Cycle and Alters Systemic Metabolism to Suppress T Cell Function. *Immunity* 51, 1074–1087.e9. [PubMed: 31784108]
17. Karagiannis F, Peukert K, Surace L, Michla M, Nikolka F, Fox M, Weiss P, Feuerborn C, Maier P, Schulz S, et al. (2022). Impaired ketogenesis ties metabolism to T cell dysfunction in COVID-19. *Nature* 609, 801–807. [PubMed: 35901960]
18. Kaech SM, and Cui W (2012). Transcriptional control of effector and memory CD8+ T cell differentiation. *Nat. Rev. Immunol.* 12, 749–761. [PubMed: 23080391]
19. Gray SM, Kaech SM, and Staron MM (2014). The interface between transcriptional and epigenetic control of effector and memory CD8<sup>+</sup> T-cell differentiation. *Immunol. Rev.* 261, 157–168. [PubMed: 25123283]
20. Henning AN, Roychoudhuri R, and Restifo NP (2018). Epigenetic control of CD8+ T cell differentiation. *Nat. Rev. Immunol.* 18, 340–356. [PubMed: 29379213]
21. Pauken KE, Sammons MA, Odorizzi PM, Manne S, Godec J, Khan O, Drake AM, Chen Z, Sen DR, Kurachi M, et al. (2016). Epigenetic stability of exhausted T cells limits durability of reinvigoration by PD-1 blockade. *Science* 354, 1160–1165. [PubMed: 27789795]
22. Man K, Gabriel SS, Liao Y, Gloury R, Preston S, Henstridge DC, Pellegrini M, Zehn D, Berberich-Siebelt F, Febbraio MA, et al. (2017). Transcription Factor IRF4 Promotes CD8+ T Cell Exhaustion and Limits the Development of Memory-like T Cells during Chronic Infection. *Immunity* 47, 1129–1141.e5. [PubMed: 29246443]
23. Philip M, Fairchild L, Sun L, Horste EL, Camara S, Shakiba M, Scott AC, Viale A, Lauer P, Merghoub T, et al. (2017). Chromatin states define tumour-specific T cell dysfunction and reprogramming. *Nature* 545, 452–456. [PubMed: 28514453]
24. Franco F, Jaccard A, Romero P, Yu Y-R, and Ho P-C (2020). Metabolic and epigenetic regulation of T-cell exhaustion. *Nat Metab* 2, 1001–1012. [PubMed: 32958939]
25. Cahill GF Jr (2006). Fuel metabolism in starvation. *Annu. Rev. Nutr.* 26, 1–22. [PubMed: 16848698]
26. Puchalska P, and Crawford PA (2017). Multi-dimensional Roles of Ketone Bodies in Fuel Metabolism, Signaling, and Therapeutics. *Cell Metab.* 25, 262–284. [PubMed: 28178565]
27. Puchalska P, and Crawford PA (2021). Metabolic and Signaling Roles of Ketone Bodies in Health and Disease. *Annu. Rev. Nutr.* 41, 49–77. [PubMed: 34633859]
28. Ruan H-B, and Crawford PA (2018). Ketone bodies as epigenetic modifiers. *Curr. Opin. Clin. Nutr. Metab. Care* 21, 260–266. [PubMed: 29697540]
29. Best JA, Blair DA, Knell J, Yang E, Mayya V, Doedens A, Dustin ML, and Goldrath AW (2013). Transcriptional insights into the CD8+ T cell response to infection and memory T cell formation. *Nat. Immunol.* 14, 404–412. [PubMed: 23396170]
30. Brenes AJ, Hukelmann JL, Spinelli L, Howden AJM, Marchingo JM, Sinclair LV, Rollings C, James OJ, Phair IR, Matthews SP, et al. (2022). The Immunological Proteome Resource. *bioRxiv*, 2022.08.29.505666.
31. Ma EH, Verway MJ, Johnson RM, Roy DG, Steadman M, Hayes S, Williams KS, Sheldon RD, Samborska B, Kosinski PA, et al. (2019). Metabolic Profiling Using Stable Isotope Tracing Reveals Distinct Patterns of Glucose Utilization by Physiologically Activated CD8+ T Cells. *Immunity* 51, 856–870.e5. [PubMed: 31747582]
32. Kaymak I, Luda KM, Duimstra LR, Ma EH, Longo J, Dahabieh MS, Faubert B, Oswald BM, Watson MJ, Kitchen-Goosen SM, et al. (2022). Carbon source availability drives nutrient utilization in CD8+ T cells. *Cell Metab.* 34, 1298–1311.e6. [PubMed: 35981545]
33. Horton JL, Davidson MT, Kurishima C, Vega RB, Powers JC, Matsuura TR, Petucci C, Lewandowski ED, Crawford PA, Muoio DM, et al. (2019). The failing heart utilizes 3-hydroxybutyrate as a metabolic stress defense. *JCI Insight* 4, e124079. [PubMed: 30668551]
34. Martin MD, Condotta SA, Harty JT, and Badovinac VP (2012). Population dynamics of naive and memory CD8 T cell responses after antigen stimulations in vivo. *J. Immunol.* 188, 1255–1265. [PubMed: 22205031]

35. Daniel B, Yost KE, Hsiung S, Sandor K, Xia Y, Qi Y, Hiam-Galvez KJ, Black M, J Raposo C, Shi Q, et al. (2022). Divergent clonal differentiation trajectories of T cell exhaustion. *Nat. Immunol.* 23, 1614–1627. [PubMed: 36289450]
36. Szabo PA, Levitin HM, Miron M, Snyder ME, Senda T, Yuan J, Cheng YL, Bush EC, Dogra P, Thapa P, et al. (2019). Single-cell transcriptomics of human T cells reveals tissue and activation signatures in health and disease. *Nat. Commun.* 10, 4706. [PubMed: 31624246]
37. Zhang H, Tang K, Ma J, Zhou L, Liu J, Zeng L, Zhu L, Xu P, Chen J, Wei K, et al. (2020). Ketogenesis-generated  $\beta$ -hydroxybutyrate is an epigenetic regulator of CD8<sup>+</sup> T-cell memory development. *Nat. Cell Biol.* 22, 18–25. [PubMed: 31871320]
38. Cantor JR, Abu-Remaileh M, Kanarek N, Freinkman E, Gao X, Louissaint A Jr, Lewis CA, and Sabatini DM. (2017). Physiologic Medium Rewires Cellular Metabolism and Reveals Uric Acid as an Endogenous Inhibitor of UMP Synthase. *Cell* 169, 258–272.e17. [PubMed: 28388410]
39. Sugimoto M, Ikeda S, Niigata K, Tomita M, Sato H, and Soga T (2012). MIMDB: Mouse Multiple Tissue Metabolome Database. *Nucleic Acids Res.* 40, D809–14. [PubMed: 22139941]
40. Lien EC, Westermark AM, Zhang Y, Yuan C, Li Z, Lau AN, Sapp KM, Wolpin BM, and Vander Heiden MG (2021). Low glycaemic diets alter lipid metabolism to influence tumour growth. *Nature* 599, 302–307. [PubMed: 34671163]
41. Gouirand V, Gicquel T, Lien EC, Jaune-Pons E, Da Costa Q, Finetti P, Metay E, Duluc C, Mayers JR, Audebert S, et al. (2022). Ketogenic HMG-CoA lyase and its product  $\beta$ -hydroxybutyrate promote pancreatic cancer progression. *EMBO J.* 41, e110466. [PubMed: 35307861]
42. Arnold PK, Jackson BT, Paras KI, Brunner JS, Hart ML, Newsom OJ, Alibeckoff SP, Endress J, Drill E, Sullivan LB, et al. (2022). A non-canonical tricarboxylic acid cycle underlies cellular identity. *Nature* 603, 477–481. [PubMed: 35264789]
43. Sheldon RD, Ma EH, DeCamp LM, Williams KS, and Jones RG (2021). Interrogating in vivo T-cell metabolism in mice using stable isotope labeling metabolomics and rapid cell sorting. *Nat. Protoc.* 16, 4494–4521. [PubMed: 34349284]
44. Vander Heiden MG, Lunt SY, Dayton TL, Fiske BP, Israelsen WJ, Mattaini KR, Vokes NI, Stephanopoulos G, Cantley LC, Metallo CM, et al. (2011). Metabolic pathway alterations that support cell proliferation. *Cold Spring Harb. Symp. Quant. Biol.* 76, 325–334. [PubMed: 22262476]
45. Röhrig F, and Schulze A (2016). The multifaceted roles of fatty acid synthesis in cancer. *Nat. Rev. Cancer* 16, 732–749. [PubMed: 27658529]
46. Barnes CE, English DM, and Cowley SM (2019). Acetylation & Co: an expanding repertoire of histone acylations regulates chromatin and transcription. *Essays Biochem.* 63, 97–107. [PubMed: 30940741]
47. Northrop JK, Thomas RM, Wells AD, and Shen H (2006). Epigenetic remodeling of the IL-2 and IFN- $\gamma$  loci in memory CD8 T cells is influenced by CD4 T cells. *J. Immunol.* 177, 1062–1069. [PubMed: 16818762]
48. Shimazu T, Hirschey MD, Newman J, He W, Shirakawa K, Le Moan N, Grueter CA, Lim H, Saunders LR, Stevens RD, et al. (2013). Suppression of oxidative stress by  $\beta$ -hydroxybutyrate, an endogenous histone deacetylase inhibitor. *Science* 339, 211–214. [PubMed: 23223453]
49. Xie Z, Zhang D, Chung D, Tang Z, Huang H, Dai L, Qi S, Li J, Colak G, Chen Y, et al. (2016). Metabolic Regulation of Gene Expression by Histone Lysine  $\beta$ -Hydroxybutyrylation. *Mol. Cell* 62, 194–206. [PubMed: 27105115]
50. Dickson BM, Tiedemann RL, Chomiak AA, Cornett EM, Vaughan RM, and Rothbart SB (2020). A physical basis for quantitative ChIP-sequencing. *J. Biol. Chem.* 295, 15826–15837. [PubMed: 32994221]
51. Cotter DG, Schugar RC, Wentz AE, d'Avignon DA, and Crawford PA (2013). Successful adaptation to ketosis by mice with tissue-specific deficiency of ketone body oxidation. *Am. J. Physiol. Endocrinol. Metab.* 304, E363–74. [PubMed: 23233542]
52. Demiroz D, Platanitis E, Bryant M, Fischer P, Prchal-Murphy M, Lercher A, Lassnig C, Baccarini M, Müller M, Bergthaler A, et al. (2021). *Listeria monocytogenes* infection rewires host metabolism with regulatory input from type I interferons. *PLoS Pathog.* 17, e1009697. [PubMed: 34237114]

53. Gormsen LC, Svart M, Thomsen HH, Søndergaard E, Vendelbo MH, Christensen N, Tolbod LP, Harms HJ, Nielsen R, Wiggers H, et al. (2017). Ketone Body Infusion With 3-Hydroxybutyrate Reduces Myocardial Glucose Uptake and Increases Blood Flow in Humans: A Positron Emission Tomography Study. *J. Am. Heart Assoc.* 6, e005066. [PubMed: 28242634]
54. Kadir AA, Stubbs BJ, Chong C-R, Lee H, Cole M, Carr C, Hauton D, McCullagh J, Evans RD, and Clarke K (2023). On the interdependence of ketone body oxidation, glycogen content, glycolysis and energy metabolism in the heart. *J. Physiol.* 601, 1207–1224. [PubMed: 36799478]
55. Cox PJ, Kirk T, Ashmore T, Willerton K, Evans R, Smith A, Murray AJ, Stubbs B, West J, McLure SW, et al. (2016). Nutritional Ketosis Alters Fuel Preference and Thereby Endurance Performance in Athletes. *Cell Metab.* 24, 256–268. [PubMed: 27475046]
56. Ma EH, Bantug G, Griss T, Condotta S, Johnson RM, Samborska B, Mainolfi N, Suri V, Guak H, Balmer ML, et al. (2017). Serine Is an Essential Metabolite for Effector T Cell Expansion. *Cell Metab.* 25, 345–357. [PubMed: 28111214]
57. Troha K, and Ayres JS (2020). Metabolic Adaptations to Infections at the Organismal Level. *Trends Immunol.* 41, 113–125. [PubMed: 31959515]
58. Hirschberger S, Strauß G, Effinger D, Marstaller X, Ferstl A, Müller MB, Wu T, Hübner M, Rahmel T, Mascolo H, et al. (2021). Very-low-carbohydrate diet enhances human T-cell immunity through immunometabolic reprogramming. *EMBO Mol. Med.* 13, e14323.
59. Puchalska P, Martin SE, Huang X, Lengfeld JE, Daniel B, Graham MJ, Han X, Nagy L, Patti GJ, and Crawford PA (2019). Hepatocyte-Macrophage Acetoacetate Shuttle Protects against Tissue Fibrosis. *Cell Metab.* 29, 383–398.e7. [PubMed: 30449686]
60. Youm Y-H, Nguyen KY, Grant RW, Goldberg EL, Bodogai M, Kim D, D’Agostino D, Planavsky N, Lupfer C, Kanneganti TD, et al. (2015). The ketone metabolite  $\beta$ -hydroxybutyrate blocks NLRP3 inflammasome-mediated inflammatory disease. *Nat. Med.* 21, 263–269. [PubMed: 25686106]
61. Goldberg EL, Asher JL, Molony RD, Shaw AC, Zeiss CJ, Wang C, Morozova-Roche LA, Herzog RI, Iwasaki A, and Dixit VD (2017).  $\beta$ -Hydroxybutyrate Deactivates Neutrophil NLRP3 Inflammasome to Relieve Gout Flares. *Cell Rep.* 18, 2077–2087. [PubMed: 28249154]
62. Goldberg EL, Molony RD, Kudo E, Sidorov S, Kong Y, Dixit VD, and Iwasaki A (2019). Ketogenic diet activates protective  $\gamma\delta$  T cell responses against influenza virus infection. *Sci Immunol* 4, eaav2026. [PubMed: 31732517]
63. Goldberg EL, Shchukina I, Asher JL, Sidorov S, Artyomov MN, and Dixit VD (2020). Ketogenesis activates metabolically protective  $\gamma\delta$  T cells in visceral adipose tissue. *Nat Metab* 2, 50–61. [PubMed: 32694683]
64. Hirschberger S, Gellert L, Effinger D, Muenchhoff M, Herrmann M, Briegel J-M, Zwißler B, and Kreth S (2022). Ketone Bodies Improve Human CD8+ Cytotoxic T-Cell Immune Response During COVID-19 Infection. *Front. Med.* 9, 923502.
65. Ferrere G, Tidjani Alou M, Liu P, Goubet A-G, Fidelle M, Kepp O, Durand S, Iebba V, Fluckiger A, Daillère R, et al. (2021). Ketogenic diet and ketone bodies enhance the anticancer effects of PD-1 blockade. *JCI Insight* 6, e145207. [PubMed: 33320838]
66. Wei R, Zhou Y, Li C, Rychahou P, Zhang S, Titlow WB, Bauman G, Wu Y, Liu J, Wang C, et al. (2022). Ketogenesis Attenuates KLF5-Dependent Production of CXCL12 to Overcome the Immunosuppressive Tumor Microenvironment in Colorectal Cancer. *Cancer Res.* 82, 1575–1588. [PubMed: 35247887]
67. Haring JS, Corbin GA, and Harty JT (2005). Dynamic regulation of IFN-gamma signaling in antigen-specific CD8+ T cells responding to infection. *J. Immunol.* 174, 6791–6802. [PubMed: 15905520]
68. Stagg J, Divisekera U, Duret H, Sparwasser T, Teng MWL, Darcy PK, and Smyth MJ (2011). CD73-deficient mice have increased antitumor immunity and are resistant to experimental metastasis. *Cancer Res.* 71, 2892–2900. [PubMed: 21292811]
69. Chen R, Bélanger S, Frederick MA, Li B, Johnston RJ, Xiao N, Liu Y-C, Sharma S, Peters B, Rao A, et al. (2014). In vivo RNA interference screens identify regulators of antiviral CD4(+) and CD8(+) T cell differentiation. *Immunity* 41, 325–338. [PubMed: 25148027]

70. Mookerjee SA, Gerencser AA, Nicholls DG, and Brand MD (2017). Quantifying intracellular rates of glycolytic and oxidative ATP production and consumption using extracellular flux measurements. *J. Biol. Chem.* 292, 7189–7207. [PubMed: 28270511]
71. Roy DG, Chen J, Mamane V, Ma EH, Muhire BM, Sheldon RD, Shorstova T, Koning R, Johnson RM, Esaulova E, et al. (2020). Methionine Metabolism Shapes T Helper Cell Responses through Regulation of Epigenetic Reprogramming. *Cell Metab.* 31, 250–266.e9. [PubMed: 32023446]
72. Luo W, Friedman MS, Shedden K, Hankenson KD, and Woolf PJ (2009). GAGE: generally applicable gene set enrichment for pathway analysis. *BMC Bioinformatics* 10, 161. [PubMed: 19473525]
73. Dobin A, Davis CA, Schlesinger F, Drenkow J, Zaleski C, Jha S, Batut P, Chaisson M, and Gingeras TR (2013). STAR: ultrafast universal RNA-seq aligner. *Bioinformatics* 29, 15–21. [PubMed: 23104886]
74. Ritchie ME, Phipson B, Wu D, Hu Y, Law CW, Shi W, and Smyth GK (2015). limma powers differential expression analyses for RNA-sequencing and microarray studies. *Nucleic Acids Res.* 43, e47. [PubMed: 25605792]
75. Love MI, Huber W, and Anders S (2014). Moderated estimation of fold change and dispersion for RNA-seq data with DESeq2. *Genome Biol.* 15, 550. [PubMed: 25516281]
76. Durinck S, Moreau Y, Kasprzyk A, Davis S, De Moor B, Brazma A, and Huber W (2005). BioMart and Bioconductor: a powerful link between biological databases and microarray data analysis. *Bioinformatics* 21, 3439–3440. [PubMed: 16082012]
77. Durinck S, Spellman PT, Birney E, and Huber W (2009). Mapping identifiers for the integration of genomic datasets with the R/Bioconductor package biomaRt. *Nat. Protoc.* 4, 1184–1191. [PubMed: 19617889]
78. Subramanian A, Tamayo P, Mootha VK, Mukherjee S, Ebert BL, Gillette MA, Paulovich A, Pomeroy SL, Golub TR, Lander ES, et al. (2005). Gene set enrichment analysis: a knowledge-based approach for interpreting genome-wide expression profiles. *Proc. Natl. Acad. Sci. U. S. A.* 102, 15545–15550. [PubMed: 16199517]
79. Wu T, Hu E, Xu S, Chen M, Guo P, Dai Z, Feng T, Zhou L, Tang W, Zhan L, et al. (2021). clusterProfiler 4.0: A universal enrichment tool for interpreting omics data. *Innovation (Camb)* 2, 100141. [PubMed: 34557778]
80. Dickson BM, Kupai A, Vaughan RM, and Rothbart SB (2022). Theoretical and practical refinements of sans spike-in quantitative ChIP-seq with application to p300/CBP inhibition. *bioRxiv*, 2022.08.09.503331.
81. Robinson JT, Thorvaldsdóttir H, Winckler W, Guttman M, Lander ES, Getz G, and Mesirov JP (2011). Integrative genomics viewer. *Nat. Biotechnol.* 29, 24–26. [PubMed: 21221095]

**Highlights**

- Ketolysis regulates CD8<sup>+</sup> T cell metabolism and effector responses *in vivo*
- Exogenous ketone bodies enhance CD8<sup>+</sup> T cell bioenergetics and cytokine production
- The ketone body  $\beta$ OHB is preferred over glucose for synthesis of acetyl-CoA
- $\beta$ OHB-derived acetyl-CoA regulates histone acetylation at effector gene loci

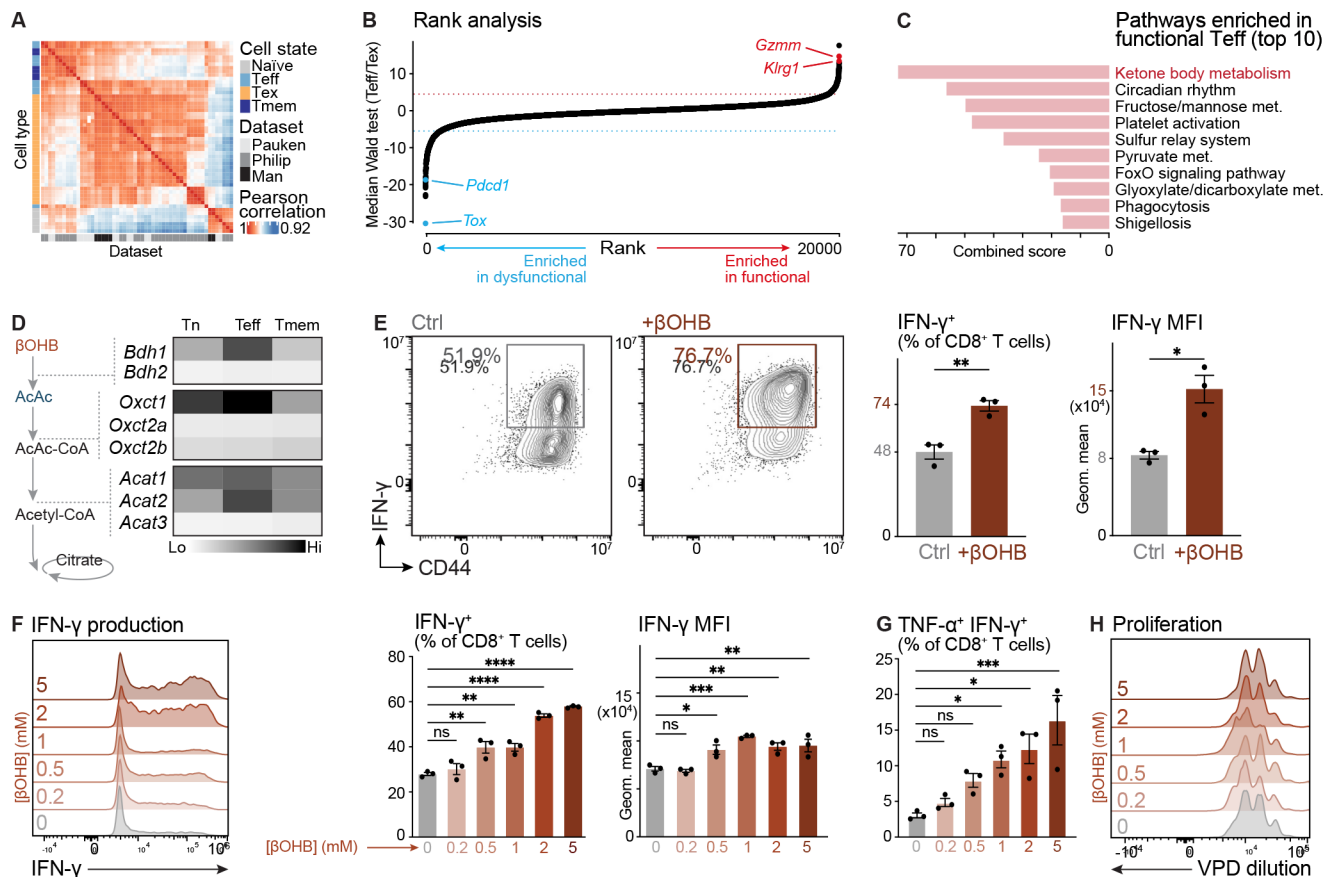


**Figure 1. Ketolysis is a metabolic feature of functional CD8 $^+$  T effector cells**

(A) Pearson correlation-driven similarity matrix analysis of gene expression profiles of CD8 $^+$  T cell states. Analysis was conducted using RNA-seq datasets from three independent studies characterizing gene expression profiles of antigen-specific CD8 $^+$  T cells in infection and tumor models *in vivo*<sup>21–23</sup>. (B) Rank analysis of genes enriched in dysfunctional versus functional CD8 $^+$  T cell states. Median Wald test statistics for differentially-expressed genes between Teff and Tex populations (Teff/Tex) were calculated based on tumor and virus response datasets. (C) Pathway analysis of the top 10 KEGG pathways enriched in functional Teff cells from (B). (D) Heatmap depicting mRNA expression of ketolysis pathway genes in naive (Tn) OT-I CD8 $^+$  T cells and *Lm*-OVA-induced Teff (2 dpi) and Tmem (30 dpi) cells<sup>29</sup>. A schematic of ketolysis is shown. (E) IFN- $\gamma$  production by CD8 $^+$  T cells activated with anti-CD3 and anti-CD28 antibodies in IMDM for 3 days in the presence (+ $\beta$ OHB) or absence (Ctrl) of 5 mM  $\beta$ OHB. *Left*, Flow cytometry plots for CD44 versus IFN- $\gamma$  expression. *Right*, Bar graphs showing the percentage of IFN- $\gamma^+$ CD8 $^+$  T cells and geometric MFI for IFN- $\gamma$ . Data represent the mean  $\pm$  SEM (n=3 mice/group). (F) IFN- $\gamma$  production by CD8 $^+$  T cells activated with anti-CD3 and anti-CD28 antibodies in VIM for 3 days  $\pm$   $\beta$ OHB (0–5 mM). *Left*, Histograms of IFN- $\gamma$  expression. *Right*, Bar graphs showing the percentage of IFN- $\gamma^+$ CD8 $^+$  T cells and the geometric MFI for IFN- $\gamma$  production. Data represent the mean  $\pm$  SEM (n=3 mice/group). Statistical significance was assessed by one-way ANOVA with Dunnett’s multiple comparisons test. (G) Bar graph showing the percentage of polyfunctional (TNF- $\alpha^+$ IFN- $\gamma^+$ ) CD8 $^+$  T cells following 3 days of

activation as described in (F). Data represent the mean  $\pm$  SEM (n=3 mice/group). Statistical significance was assessed by one-way ANOVA with Dunnett's multiple comparisons test.

**(H)** Histograms of violet proliferation dye (VPD) dilution in CD8<sup>+</sup> T cells following 3 days of activation as described in (F) (n=3).

Author Manuscript

Author Manuscript

Author Manuscript

Author Manuscript

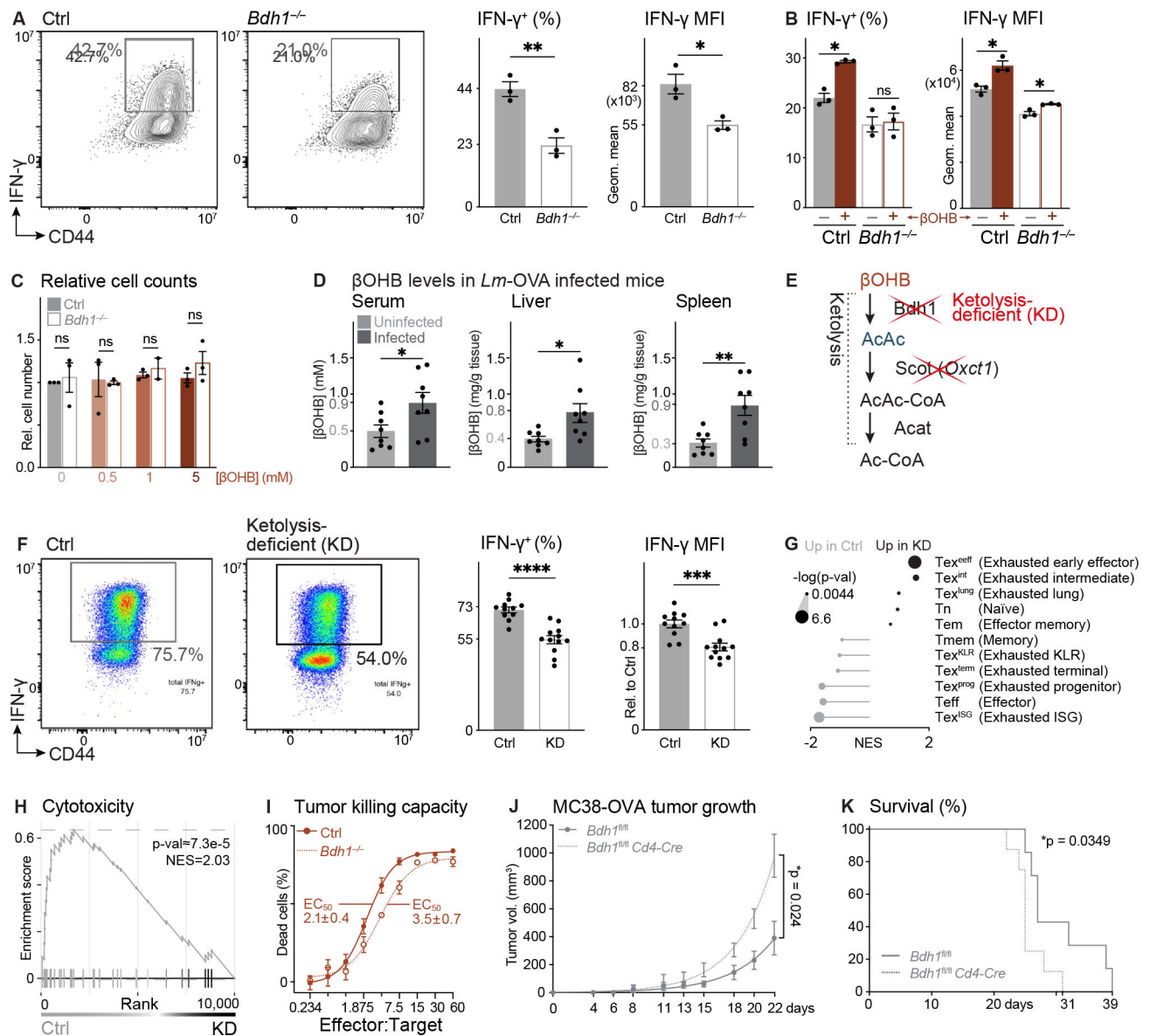


**Figure 2. CD8<sup>+</sup> T cell-intrinsic ketolysis is required for optimal effector function**

(A) IFN- $\gamma$  production by activated control (Ctrl) and *Bdh1<sup>-/-</sup>* CD8<sup>+</sup> T cells isolated from *Bdh1<sup>fl/fl</sup>* and *Bdh1<sup>fl/fl</sup> Cd4-Cre* mice, respectively. T cells were activated with anti-CD3 and anti-CD28 antibodies in IMDM for 3 days. *Left*, Flow cytometry plots for CD44 versus IFN- $\gamma$  expression. *Right*, Bar graphs showing the percentage of IFN- $\gamma^+$ CD8<sup>+</sup> T cells and the geometric MFI for IFN- $\gamma$  production. Data represent the mean  $\pm$  SEM (n=3 mice/group). (B) Bar graphs showing the percentage of IFN- $\gamma^+$ CD8<sup>+</sup> T cells and the geometric MFI for IFN- $\gamma$  in Ctrl and *Bdh1<sup>-/-</sup>* CD8<sup>+</sup> T cells following 3 days of activation in VIM  $\pm$  5 mM  $\beta$ OHB. Data represent the mean  $\pm$  SEM (n=3 mice/group). (C) Cell counts for activated Ctrl and *Bdh1<sup>-/-</sup>* CD8<sup>+</sup> T cells after 48 h of culture in VIM  $\pm$   $\beta$ OHB (normalized to Ctrl cells cultured without  $\beta$ OHB). Data represent the mean  $\pm$  SEM (n=3 mice/group). (D)  $\beta$ OHB concentrations in the serum, liver, and spleen of mock-infected (uninfected) and attenuated *Lm*-OVA-infected mice 2 dpi. Data represent the mean  $\pm$  SEM (n=8 mice/group). (E)

Schematic defining ketolysis-deficient (KD) CD8<sup>+</sup> T cells. *Bdh1*<sup>-/-</sup> T cells were transduced with an *Oxct1*-targeting shRNA to generate T cells that are unable to oxidize either βOHB or AcAc. (F) IFN-γ production by Ctrl and KD OT-I CD8<sup>+</sup> T cells isolated from *Lm*-OVA-infected mice 7 dpi. *Left*, Flow cytometry plots for CD44 versus IFN-γ expression. *Right*, Percentage of IFN-γ<sup>+</sup> OT-I CD8<sup>+</sup> T cells and relative geometric MFI of IFN-γ expression (normalized to Ctrl cells). Data represent the mean ± SEM (n=11–12 mice/group). (G) Normalized enrichment scores (NES) of transcriptional signatures associated with CD8<sup>+</sup> T cell subsets<sup>35</sup> compared to the differentially-expressed genes in KD versus Ctrl OT-I CD8<sup>+</sup> T cells responding to *Lm*-OVA (7 dpi). (H) GSEA of CD8<sup>+</sup> T cell cytotoxicity genes<sup>36</sup> in Ctrl versus KD OT-I CD8<sup>+</sup> T cells responding to *Lm*-OVA (7 dpi). (I) Percentage of dead MC38-OVA cancer cells after 24 h of co-culture with activated Ctrl or *Bdh1*<sup>-/-</sup> OT-I CD8<sup>+</sup> T cells at the indicated effector:target (E:T) ratio. The E:T ratio required to kill 50% of cancer cells (EC<sub>50</sub>) for each genotype is indicated. Data represent the mean ± SD (n=3/group). (J) MC38-OVA tumor growth in *Bdh1*<sup>fl/fl</sup> and *Bdh1*<sup>fl/fl</sup>*Cd4-Cre* mice. Data represent the mean ± SEM (n=5 mice/group). Statistical significance was assessed by two-way ANOVA. (K) Kaplan-Meier curve of time to humane endpoint for MC38-OVA tumor-bearing *Bdh1*<sup>fl/fl</sup> and *Bdh1*<sup>fl/fl</sup>*Cd4-Cre* mice (7–8 mice/group). Statistical significance was assessed by log-rank test.

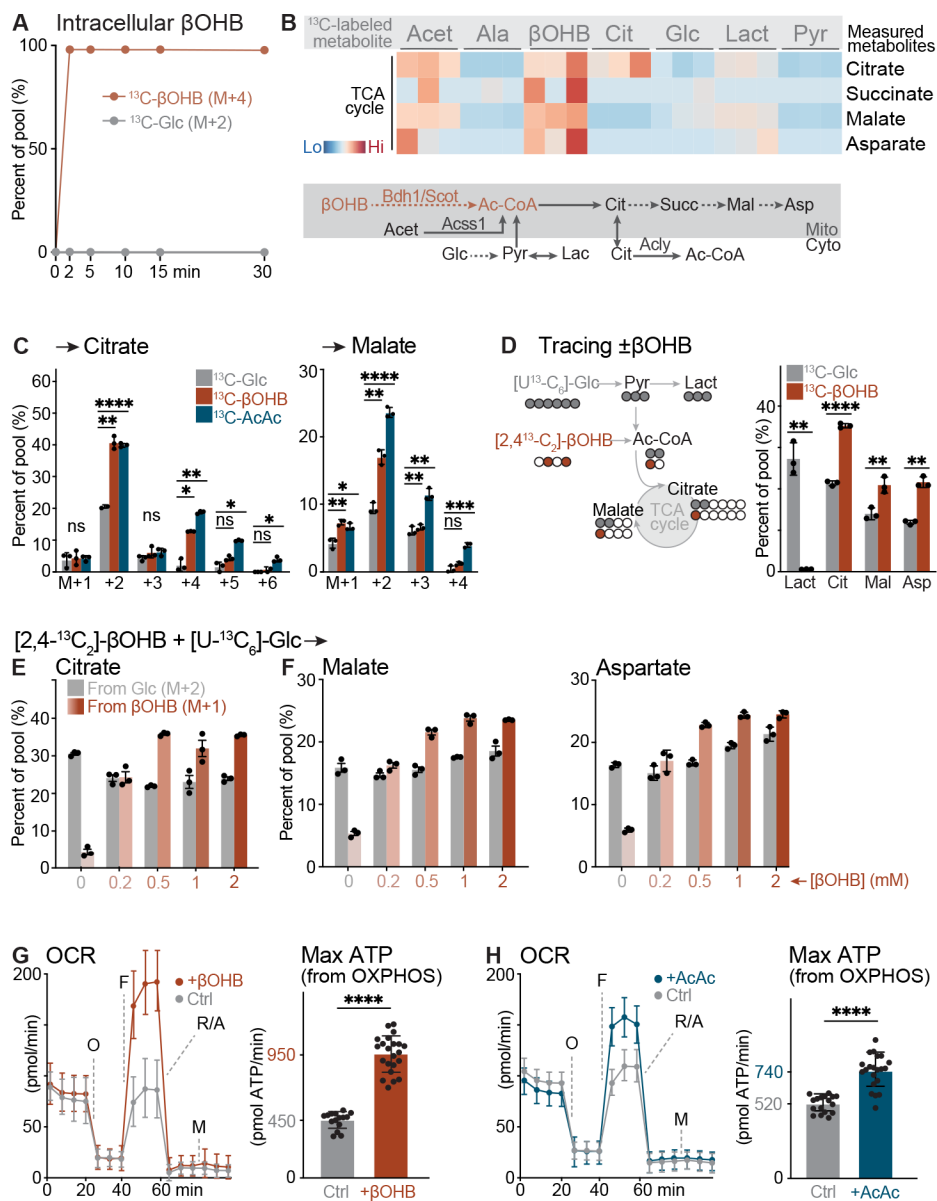


**Figure 3. KBs fuel the TCA cycle in CD8<sup>+</sup> T cells**

(A) Timecourse of  $\beta$ OHB uptake and cell-intrinsic  $\beta$ OHB production from glucose in activated CD8<sup>+</sup> T cells. Shown is the contribution of 0.85 mM [ $^{13}\text{C}_4$ ]- $\beta$ OHB (M+4, from exogenous [ $^{13}\text{C}_4$ ]- $\beta$ OHB) or 5 mM [ $^{13}\text{C}_6$ ]-glucose-derived  $\beta$ OHB (M+2) to the overall intracellular  $\beta$ OHB pool over time. Data represent the mean  $\pm$  SD (n=3/group). (B) Heatmap representing the relative incorporation of  $^{13}\text{C}$  into TCA cycle metabolites derived from the indicated  $^{13}\text{C}$ -labeled substrates. Shown is a schematic depicting the contribution of different carbon sources to TCA cycle metabolism, with enzymes and reactions localized to the cytosol and mitochondrion indicated. (C) Mass isotopologue distribution (MID) for 5 mM [ $^{13}\text{C}_6$ ]-glucose-, 2 mM [ $^{13}\text{C}_4$ ]- $\beta$ OHB-, or 2 mM [ $^{13}\text{C}_4$ ]-AcAc-derived carbon into citrate and malate in activated CD8<sup>+</sup> T cells after 2 h of culture. Data represent the mean  $\pm$  SD (n=3/group). Statistical significance was assessed by one-way ANOVA with

Dunnett's multiple comparisons test. **(D)** Activated CD8<sup>+</sup> Teff cells were cultured in VIM containing both 5 mM [U-<sup>13</sup>C<sub>6</sub>]-glucose and 2 mM [2,4-<sup>13</sup>C<sub>2</sub>]-βOHB for 2 h, and the relative contribution of <sup>13</sup>C label from [U-<sup>13</sup>C<sub>6</sub>]-glucose (M+2) or [2,4-<sup>13</sup>C<sub>2</sub>]-βOHB (M+1) to TCA cycle metabolite pools is shown. Lactate labeling from [U-<sup>13</sup>C<sub>6</sub>]-glucose (M+3) or [2,4-<sup>13</sup>C<sub>2</sub>]-βOHB (M+1) is shown as a control. Data represent the mean ± SD (n=3/group). **(E-F)** Relative contribution of <sup>13</sup>C label from [U-<sup>13</sup>C<sub>6</sub>]-glucose (M+2) or [2,4-<sup>13</sup>C<sub>2</sub>]-βOHB (M+1) into the intracellular **(E)** citrate or **(F)** malate and aspartate pools in CD8<sup>+</sup> T cells. Cells were cultured for 2 h in VIM containing 5 mM [U-<sup>13</sup>C<sub>6</sub>]-glucose and the indicated concentration of [2,4-<sup>13</sup>C<sub>2</sub>]-βOHB. Data represent the mean ± SEM (n=3 mice/group). **(G-H)** Bioenergetic profile of *in vitro*-activated CD8<sup>+</sup> T cells cultured with **(G)** 2 mM βOHB or **(H)** 2 mM AcAc. *Left*, Oxygen consumption rate (OCR) plots for activated T cells over time for βOHB and AcAc. Time of addition of oligomycin (O), FCCP (F), rotenone and antimycin A (R/A), and monensin (M) are indicated. *Right*, Maximal ATP production rates from OXPHOS following addition of βOHB or AcAc. T cells that received no exogenous KB substrate (Ctrl) are indicated. Data represent the mean ± SD (n=15–22/group).

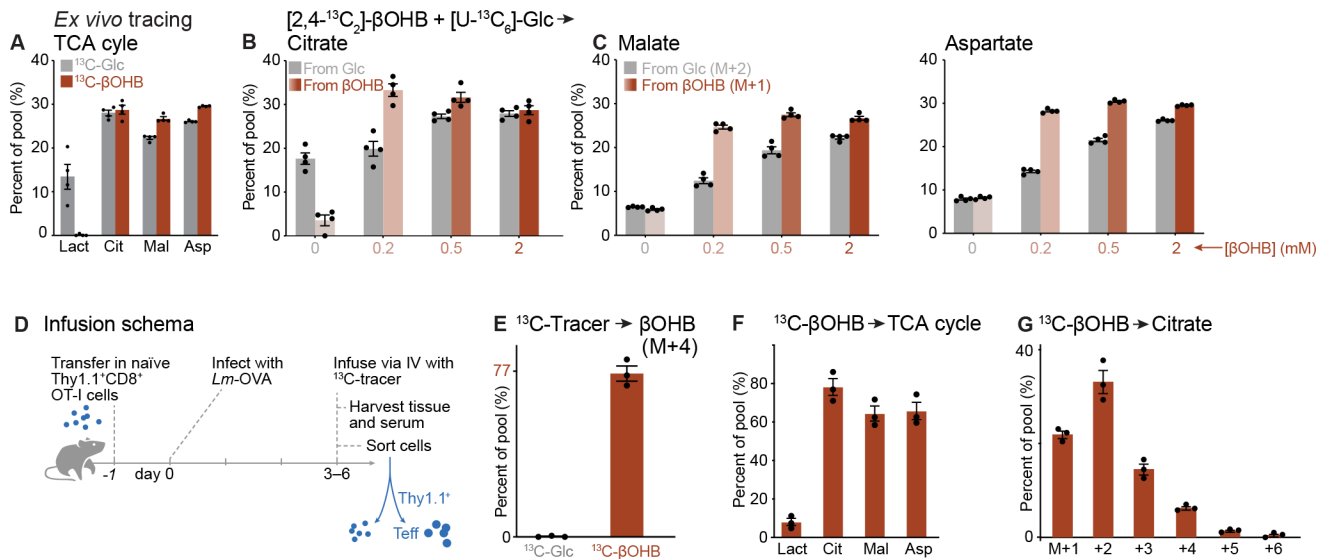


### Figure 4. $\beta$ OHB is a physiologic fuel for $CD8^+$ T cells

(A) Direct comparison of TCA cycle labeling from  $\beta$ OHB and glucose using the competitive tracing strategy described in Figure 3D.  $Thy1.1^+OT-I CD8^+$  T cells were isolated from *Lm-OVA*-infected mice (7 dpi) and cultured *ex vivo* for 2 h in VIM containing 5 mM  $[U-^{13}C_6]$ -glucose and 2 mM  $[2,4-^{13}C_2]$ - $\beta$ OHB. Data are presented as in Figure 3D and represent the mean  $\pm$  SEM (n=4 biological replicates). (B-C)  $Thy1.1^+OT-I CD8^+$  T cells isolated from *Lm-OVA*-infected mice (7 dpi) were cultured *ex vivo* for 2 h in VIM containing 5 mM  $[U-^{13}C_6]$ -glucose and the indicated concentration of  $[2,4-^{13}C_2]$ - $\beta$ OHB. Relative contribution of  $^{13}C$  label from  $[U-^{13}C_6]$ -glucose (M+2) or  $[2,4-^{13}C_2]$ - $\beta$ OHB (M+1) to the intracellular (B) citrate or (C) malate and aspartate pools in *Lm-OVA*-specific OT-I  $CD8^+$  T cells. Data represent the mean  $\pm$  SEM (n=4 biological replicates). (D) Schematic of experimental set up for  $^{13}C$  infusions in attenuated *Lm-OVA*-infected mice using  $[U-^{13}C_4]$ - $\beta$ OHB or  $[U-^{13}C_6]$ -glucose. (E) Relative contribution of infused  $[U-^{13}C_6]$ -glucose or  $[U-^{13}C_4]$ - $\beta$ OHB to the intracellular  $\beta$ OHB (M+4) pool in *Lm-OVA*-specific OT-I  $CD8^+$  T cells (6 dpi). Data represent the mean  $\pm$  SEM (n=3 mice/group).  $^{13}C$  metabolite enrichment was normalized relative to steady-state  $[U-^{13}C_6]$ -glucose (M+6) or  $[U-^{13}C_4]$ - $\beta$ OHB (M+4) enrichment in serum. (F-G) Enrichment of infused  $[U-^{13}C_4]$ - $\beta$ OHB-derived carbon into intracellular metabolites in *Lm-OVA*-specific OT-I  $CD8^+$  T cells (6 dpi).  $^{13}C$  metabolite enrichment was normalized relative to steady-state  $[U-^{13}C_4]$ - $\beta$ OHB (M+4) enrichment in serum. Data represent the mean  $\pm$  SEM (n=3 mice/group). (F) Percent of  $^{13}C$  enrichment from  $[U-^{13}C_4]$ - $\beta$ OHB in intracellular lactate, citrate, malate, and aspartate pools. (G) MID of  $[U-^{13}C_4]$ - $\beta$ OHB-derived carbon in intracellular citrate.

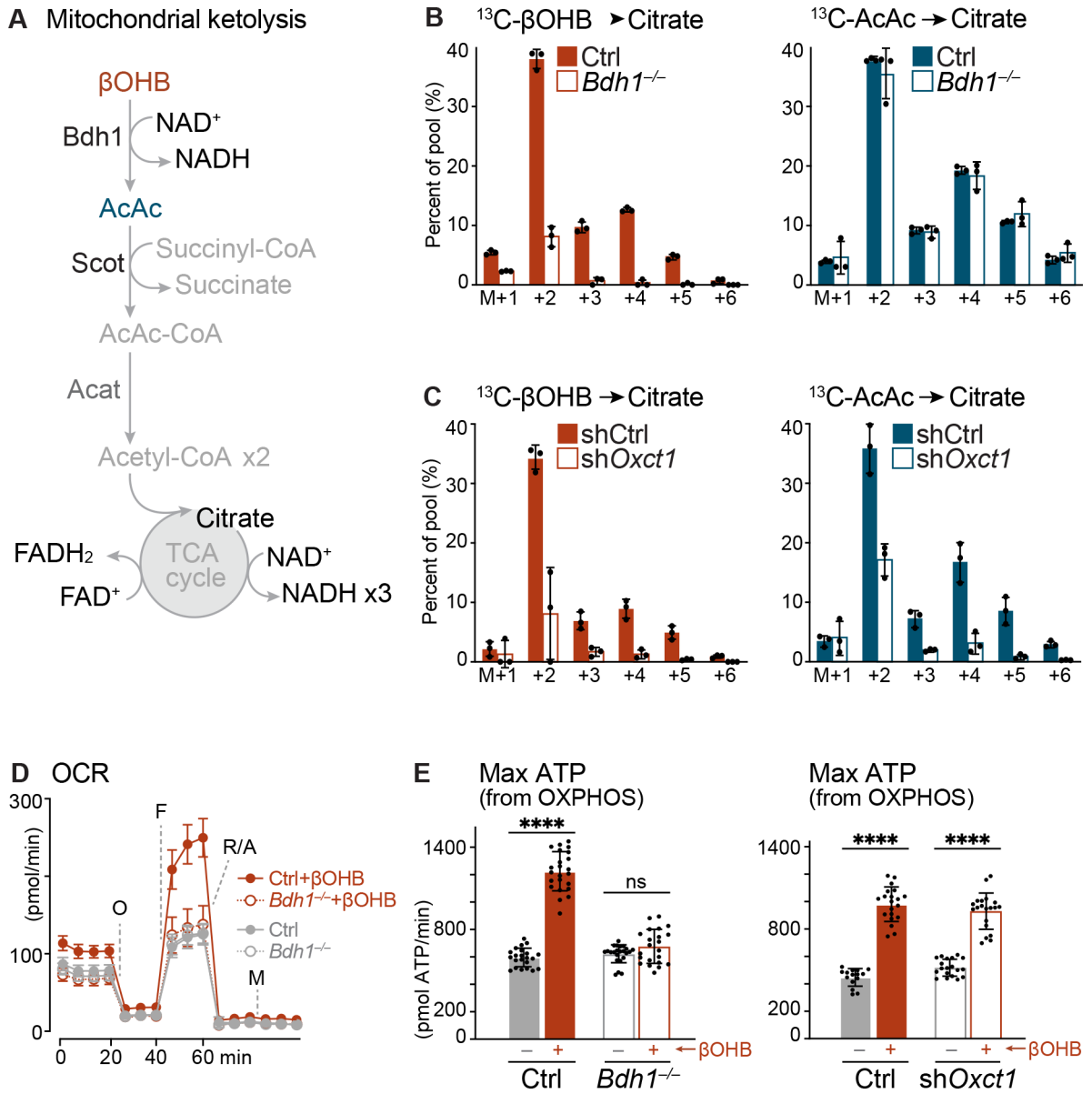


**Figure 5. BDH1 mediates the bioenergetic effects of ketolysis in CD8<sup>+</sup> T cells**

(A) Illustration of the mitochondrial ketolysis pathway. (B) Relative contribution of  $^{13}\text{C}$  label from 2 mM [U- $^{13}\text{C}_4$ ]- $\beta\text{OHB}$  (left) or 2 mM [U- $^{13}\text{C}_4$ ]-AcAc (right) to intracellular citrate in activated control (Ctrl) or *Bdh1*<sup>-/-</sup> CD8<sup>+</sup> T cells after 2 h of culture. Data represent the mean  $\pm$  SD (n=3/group). (C) Relative contribution of  $^{13}\text{C}$  label from 2 mM [U- $^{13}\text{C}_4$ ]- $\beta\text{OHB}$  (left) or 2 mM [U- $^{13}\text{C}_4$ ]-AcAc (right) to intracellular citrate in activated CD8<sup>+</sup> T cells expressing a control (shCtrl) or *Oxct1*-targeting (sh*Oxct1*) shRNA after 2 h of culture. Data represent the mean  $\pm$  SD (n=3/group). (D-E) Bioenergetic profile of *Bdh1*<sup>-/-</sup> or sh*Oxct1*-expressing CD8<sup>+</sup> T cells. (D) Oxygen consumption rate (OCR) plot over time for activated Ctrl or *Bdh1*<sup>-/-</sup> T cells cultured for 2 h  $\pm$  2 mM  $\beta\text{OHB}$ . Time of addition of oligomycin (O), FCCP (F), rotenone and antimycin A (R/A), and monensin (M) are indicated. (E) Maximal ATP production rates from OXPHOS in activated *Bdh1*<sup>-/-</sup> (left) or

sh*Oxct1*-expressing (*right*) T cells and respective controls (Ctrl) following addition of 2 mM  $\beta$ OHB for 2 h. Data represent the mean  $\pm$  SD (n=15–25/group).

Author Manuscript

Author Manuscript

Author Manuscript

Author Manuscript

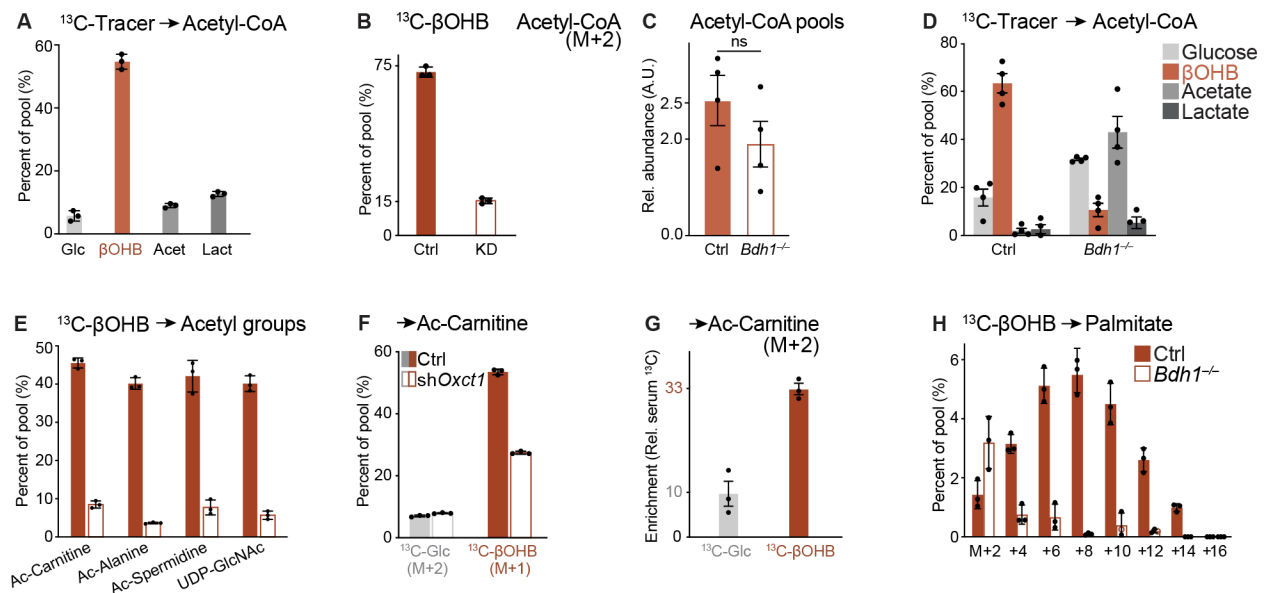


**Figure 6.  $\beta\text{OHB}$  is a major substrate for acetyl-CoA production in CD8<sup>+</sup> T cells**

(A) Production of acetyl-CoA in CD8<sup>+</sup> T cells. *Left*, Percent enrichment of [U- $^{13}\text{C}_2$ ]-acetate, [U- $^{13}\text{C}_4$ ]- $\beta\text{OHB}$ , [U- $^{13}\text{C}_6$ ]-glucose, or [U- $^{13}\text{C}_3$ ]-lactate in the intracellular acetyl-CoA (M+2) pool of activated CD8<sup>+</sup> T cells following 24 h of culture in VIM + PCS. Data represent the mean  $\pm$  SD (n=3/group). (B) Percent enrichment of 2 mM [U- $^{13}\text{C}_4$ ]- $\beta\text{OHB}$  in the acetyl-CoA (M+2) pool in control (Ctrl) and ketolysis-deficient (KD) CD8<sup>+</sup> T cells after 24 h of culture. Data represent the mean  $\pm$  SD (n=3/group). (C) Acetyl-CoA pool size in Ctrl and *Bdh1*<sup>-/-</sup> CD8<sup>+</sup> T cells cultured in VIM + PCS for 24 h. Data represent the mean  $\pm$  SEM (n=4 mice/group). A.U., arbitrary unit. (D) Percent enrichment of [U- $^{13}\text{C}_2$ ]-acetate, [U- $^{13}\text{C}_4$ ]- $\beta\text{OHB}$ , [U- $^{13}\text{C}_6$ ]-glucose, or [U- $^{13}\text{C}_3$ ]-lactate in the intracellular acetyl-CoA (M+2) pool of activated Ctrl and *Bdh1*<sup>-/-</sup> CD8<sup>+</sup> T cells following 24 h of culture in VIM + PCS. Data represent the mean  $\pm$  SEM (n=4 mice/group). (E) Percent enrichment of 2 mM [U- $^{13}\text{C}_4$ ]- $\beta\text{OHB}$  carbon in acetylated (M+2) metabolites from Ctrl and *Bdh1*<sup>-/-</sup> CD8<sup>+</sup> T cells after 24 h of culture. Data represent the mean  $\pm$  SD (n=3/group). (F) Relative  $^{13}\text{C}$  contribution from 5 mM [U- $^{13}\text{C}_6$ ]-glucose (M+2) or 2 mM [2,4- $^{13}\text{C}_2$ ]- $\beta\text{OHB}$  (M+1) to the acetyl-carnitine pool in activated CD8<sup>+</sup> T cells expressing a control (Ctrl) or *Oxct1*-targeting (sh*Oxct1*) shRNA after 2 h of culture. Data represent the mean  $\pm$  SD (n=3/group). (G) Enrichment of  $^{13}\text{C}$  carbon from 5 mM [U- $^{13}\text{C}_6$ ]-glucose or 2 mM [U- $^{13}\text{C}_4$ ]- $\beta\text{OHB}$  in acetyl-carnitine (M+2) in OT-I CD8<sup>+</sup> T cells following 2 h infusion of *Lm*-OVA-infected mice (6 dpi, as in Figure 4D). Enrichment was normalized relative to steady-state [U- $^{13}\text{C}_6$ ]-glucose (M+6) and [U- $^{13}\text{C}_4$ ]- $\beta\text{OHB}$  (M+4) enrichment in serum, respectively. Data represent the mean  $\pm$  SEM (n=3 mice/group). (H) MID of [U- $^{13}\text{C}_4$ ]- $\beta\text{OHB}$ -derived  $^{13}\text{C}$  in palmitate in activated Ctrl and *Bdh1*<sup>-/-</sup> CD8<sup>+</sup> T cells after 24 h of culture. Data represent the mean  $\pm$  SD (n=3/group).

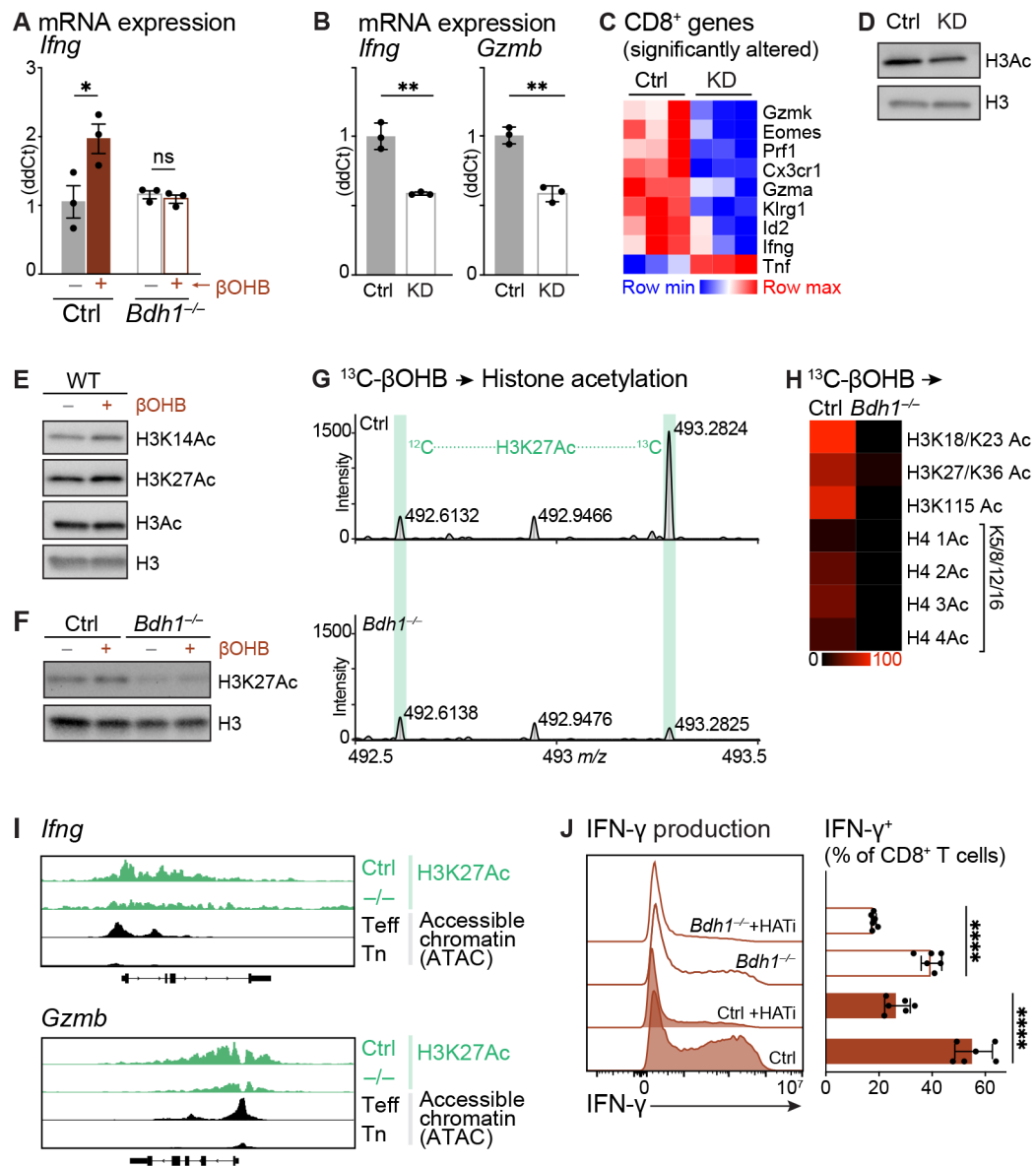


**Figure 7.  $\beta$ OHB alters histone acetylation in CD8<sup>+</sup> T cells**

(A) Relative abundance of *Ifng* mRNA in control (Ctrl) and *Bdh1*<sup>-/-</sup> CD8<sup>+</sup> T cells activated for 3 days in the presence (+) or absence (-) of 5 mM  $\beta$ OHB. Data represent the mean  $\pm$  SEM (n=3 mice/group). (B) Relative abundance of *Ifng* and *Gzmb* mRNA in activated Ctrl and ketolysis-deficient (KD) OT-I CD8<sup>+</sup> T cells. Data represent the mean  $\pm$  SD (n=3/group). (C) Heatmap of differentially-expressed effector gene transcripts ( $p < 0.05$ ) altered in Ctrl and KD OT-I CD8<sup>+</sup> Teff cells isolated from *Lm*-OVA-infected mice 7 dpi (n=3 mice/group). (D) Immunoblot of acetylated histone H3 in lysates from activated Ctrl and KD OT-I CD8<sup>+</sup> T cells. Total H3 is shown as a control for protein loading. (E) Immunoblot of global histone H3 acetylation (H3Ac) and specific acetylation at Lys14 (H3K14Ac) and Lys27 (H3K27Ac) in activated wild type (WT) CD8<sup>+</sup> T cells  $\pm$  5 mM  $\beta$ OHB for 24 h. (F) Immunoblot for H3 and H3K27Ac in activated Ctrl and *Bdh1*<sup>-/-</sup> CD8<sup>+</sup> T cells  $\pm$  5 mM  $\beta$ OHB for 24 h. (G) Mass spectra of histone H3 (peptide 27–40) from activated Ctrl or *Bdh1*<sup>-/-</sup> CD8<sup>+</sup> T cells

cultured with 5 mM [U-<sup>13</sup>C<sub>4</sub>]-βOHB for 24 h. Peaks corresponding to unlabeled (<sup>12</sup>C) and <sup>13</sup>C-labeled H3K27Ac peptides are highlighted in green. Data are representative of technical triplicates. **(H)** Heatmap quantifying [U-<sup>13</sup>C<sub>4</sub>]-βOHB-derived acetylation of histones H3 and H4 from activated Ctrl and *Bdh1*<sup>-/-</sup> CD8<sup>+</sup> T cells cultured with 5 mM [U-<sup>13</sup>C<sub>4</sub>]-βOHB for 24 h. For histone H4, the number of acetylated lysine residues on peptides containing Lys5/8/12/16 are quantified individually. **(I)** Data tracks for H3K27Ac peak enrichment at *Ifng* and *Gzmb* gene loci for 24 h-activated Ctrl and *Bdh1*<sup>-/-</sup> CD8<sup>+</sup> T cells. H3K27Ac peak enrichment is shown in green, with ATAC-seq tracks highlighting regions of chromatin accessibility in *in vivo* Tn and Teff cells<sup>23</sup> shown in black. Data are representative of duplicate samples. **(J)** IFN-γ production by Ctrl or *Bdh1*<sup>-/-</sup> CD8<sup>+</sup> T cells in the presence or absence of the HAT inhibitor (HATi) A485. Ctrl and *Bdh1*<sup>-/-</sup> CD8<sup>+</sup> T cells were activated for 3 days as in Figure 1F in VIM containing 2 mM βOHB. A485 (1 μM) was added 4 h prior to restimulation with PMA/ionomycin. *Left*, Histograms of IFN-γ expression. *Right*, Bar graph showing the percentage of IFN-γ<sup>+</sup>CD8<sup>+</sup> T cells. Data represent the mean ± SD (n=6 technical replicates from 2 mice).

## KEY RESOURCES TABLE

| REAGENT or RESOURCE  | SOURCE         | IDENTIFIER            |
|--|----------------|-----------------------|
| <b>Antibodies</b>  |                |                       |
| Hamster monoclonal anti-mouse CD3e   | eBioscience    | Clone 145-2C11        |
| Hamster monoclonal anti-mouse CD28   | eBioscience    | Clone 37.51           |
| Rat monoclonal anti-mouse CD4  | eBioscience    | Clone RM4-5           |
| Rat monoclonal anti-mouse IFN-gamma  | eBioscience    | Clone XMG1.2          |
| Rat monoclonal anti-mouse CD8  | eBioscience    | Clone 53-6.7          |
| Rat monoclonal anti-mouse TNF-alpha  | eBioscience    | Clone MP6-XT22        |
| Rat monoclonal anti-mouse CD44   | eBioscience    | Clone IM7             |
| Hamster monoclonal anti-mouse CD69   | eBioscience    | Clone H1.2F3          |
| Hamster monoclonal anti-mouse KLRG1  | eBioscience    | Clone 2F1             |
| Rat monoclonal anti-mouse CD127 (IL-7R)  | BioLegend      | Clone A7R34           |
| Mouse monoclonal anti-mouse CD90.1 (Thy-1.1)   | eBioscience    | Clone HIS51           |
| Mouse monoclonal anti-mouse CD45.1   | BioLegend      | Clone A20             |
| Mouse monoclonal anti-mouse CD45.2   | BioLegend      | Clone 104             |
| Mouse monoclonal anti-CX3CR1   | BioLegend      | Clone SA011F11        |
| Rat monoclonal anti-CD366 (Tim-3)  | BioLegend      | Clone RMT3-23         |
| Mouse monoclonal anti-Ly108 (Slamf6)   | BioLegend      | Clone 330-AJ          |
| Rabbit polyclonal anti-BDH1  | Protein Tech   | 15417-1-AP            |
| Rabbit polyclonal anti-OXCT1   | Protein Tech   | 12175-1-AP            |
| Rabbit polyclonal anti-human/mouse $\beta$ -actin  | Cell Signaling | #4967                 |
| Rabbit polyclonal anti- $\beta$ -Tubulin   | Cell Signaling | #2146                 |
| Rabbit monoclonal anti-histone 3 (H3)  | Cell Signaling | #4499; Clone D1H2     |
| Rabbit polyclonal anti-acetyl histone H3   | Millipore      | 06-599                |
| Rabbit monoclonal anti-acetyl histone H3 (Lys 9)   | Cell Signaling | #9649; Clone C5B11    |
| Rabbit monoclonal anti-acetyl histone H3 (Lys 14)  | Cell Signaling | #7627; Clone D4B9     |
| Rabbit monoclonal anti-acetyl histone H3 (Lys 18)  | Cell Signaling | #13998; Clone D8Z5H   |
| Rabbit polyclonal anti-acetyl histone H3 (Lys 23)  | Cell Signaling | #9674                 |
| Rabbit monoclonal anti-acetyl histone H3 (Lys 27)  | Cell Signaling | #8173; Clone D5E4     |
| Rabbit polyclonal anti-acetyl histone H3 (Lys 27)  | Active Motif   | #39133; Lot: 16119013 |
| HRP-conjugated goat anti-rabbit IgG antibody   | Cell Signaling | #7074                 |
| <b>Bacterial and Virus Strains</b>   |                |                       |
| Attenuated ( actA) <i>Lm</i> -OVA  | John Harty     | 67                    |
| Virulent <i>Lm</i> -OVA  | John Harty     | 34                    |
| <b>Chemicals, Peptides, and Recombinant Proteins</b>   |                |                       |
| DMEM with 4.5 g/L glucose and L-glutamine, without sodium pyruvate   | Wisent Inc.    | 319-015-CL            |
| IMDM with L-glutamine & 25 mM HEPES  | Wisent Inc.    | 319-105-CL            |
| IMDM with HEPES, without glucose, L-glutamine, L-serine, glycine, L-alanine, L-threonine, L-methionine, aspartic acid, glutamic acid, or sodium pyruvate | Wisent Inc.    | Custom                |

| REAGENT or RESOURCE  | SOURCE               | IDENTIFIER              |
|--|----------------------|-------------------------|
| Seahorse XF base medium, without phenol red                        | Agilent technologies | 103335-100              |
| Nu-Serum IV Culture Supplement                                     | Corning              | 355504; Lot 2080003     |
| Fetal bovine serum (FBS), heat-inactivated                         | Corning              | 35-016-CV; Lot 16821001 |
| Fetal bovine serum (FBS), dialyzed                                 | Corning              | 35-071-CV; Lot 35071105 |
| Pen Strep (5,000 Units/mL penicillin and 5,000 µg/mL streptomycin) | Gibco                | 15070063                |
| 2-mercaptoethanol (55 mM; 1000x)                                   | Gibco                | 21985023                |
| Recombinant murine IL-2  | Peprtech             | 212-12                  |
| Phorbol 12-myristate 13-acetate (PMA)                              | Sigma-Aldrich        | P-8139                  |
| Ionomycin  | Sigma-Aldrich        | 10634                   |
| D-Glucose [ <sup>13</sup> C <sub>6</sub> ]                         | Cambridge Isotopes   | CLM-1396                |
| Sodium D-3-hydroxybutyrate [ <sup>13</sup> C <sub>4</sub> ]        | Cambridge Isotopes   | CLM-3853                |
| Sodium D-3-hydroxybutyrate [2,4- <sup>13</sup> C <sub>2</sub> ]    | Cambridge Isotopes   | CLM-3706-1              |
| Ethyl acetoacetate [ <sup>13</sup> C <sub>4</sub> ]                | Cambridge Isotopes   | CLM-3297                |
| Sodium acetate [ <sup>13</sup> C <sub>2</sub> ]                    | Cambridge Isotopes   | CLM-440                 |
| Sodium lactate [ <sup>13</sup> C <sub>3</sub> ]                    | Cambridge Isotopes   | CLM-10768               |
| L-Alanine [ <sup>13</sup> C <sub>3</sub> ]                         | Cambridge Isotopes   | CLM-2184                |
| Sodium pyruvate [ <sup>13</sup> C <sub>3</sub> ]                   | Cambridge Isotopes   | CLM-2440                |
| Citric acid [ <sup>13</sup> C <sub>6</sub> ]                       | Sigma-Aldrich        | 606081                  |
| D-Glucose  | Sigma-Aldrich        | G8270                   |
| L-Glutamine  | Sigma-Aldrich        | G3126                   |
| L-Serine   | Sigma-Aldrich        | S4500                   |
| Glycine  | Sigma-Aldrich        | G7126                   |
| L-Alanine  | Sigma-Aldrich        | A7627                   |
| L-Threonine  | Sigma-Aldrich        | T8625                   |
| L-Methionine   | Sigma-Aldrich        | M9625                   |
| L-Aspartic acid  | Sigma-Aldrich        | A9256                   |
| L-Glutamic acid  | Sigma-Aldrich        | G1251                   |
| Sodium pyruvate  | Sigma-Aldrich        | P2256                   |
| (R)-(-)-3-Hydroxybutyric acid sodium salt                          | Sigma-Aldrich        | 298360                  |
| Sodium acetate   | Sigma-Aldrich        | S5636                   |
| Sodium citrate   | Supelco              | PHR1416                 |
| Sodium L-lactate   | Sigma-Aldrich        | L7022                   |
| Ethyl acetoacetate   | Sigma-Aldrich        | W241512                 |
| Fixable Viability Dye eFluor 506                                   | eBioscience          | 65-0866-14              |
| Fixable Viability Dye eFluor 780                                   | eBioscience          | 65-0865-14              |
| Violet Proliferation Dye 450                                       | BD Biosciences       | 562158                  |
| BD GolgiStop   | BD Biosciences       | 51-2092KZ               |
| Foxp3/Transcription factor staining buffer set                     | eBioscience          | 00-5523-00              |

| REAGENT or RESOURCE   | SOURCE                | IDENTIFIER  |
|---|-----------------------|-------------|
| Formaldehyde (16%), methanol free   | Polysciences          | 18814-20    |
| Hexadimethrine bromide (Polybrene)  | Sigma-Aldrich         | 107689      |
| OVA <sub>257-264</sub> (SIINFEKL) peptide   | AnaSpec               | AS-60193-1  |
| Universal SYBR green supermix   | Bio-Rad               | 1725271     |
| Lenti-X concentrator  | Takara Bio            | 631232      |
| cOmplete, EDTA-free (protease inhibitor cocktail tablets)   | Roche                 | 11873580001 |
| PhosSTOP (phosphatase inhibitor cocktail tablets)   | Roche                 | 4906845001  |
| p300/CBP HAT domain inhibitor (A 485)   | Tocris                | 6387        |
| Monensin sodium salt  | Sigma-Aldrich         | M5273       |
| <b>Critical Commercial Assays</b>   |                       |             |
| EasySep mouse T cell isolation kit  | StemCell technologies | #19851A     |
| EasySep mouse CD8+ T cell isolation kit   | StemCell technologies | #19853A     |
| EasySep mouse naïve CD8+ T cell isolation kit   | StemCell technologies | #19858A     |
| EasySep mouse CD90.1 positive selection kit   | StemCell technologies | #18958      |
| Qiagen RNAeasy kit  | Qiagen                | #74106      |
| Seahorse XFe96 FluxPak  | Agilent technologies  | #102416-100 |
| Seahorse XF cell mito stress test kit   | Agilent technologies  | #103015-100 |
| Histone extraction kit  | Abcam                 | ab113476    |
| High-capacity cDNA reverse transcriptase kit  | Life Technologies     | #4368814    |
| DNase digestion kit   | Qiagen                | #79254      |
| Autokit total ketone bodies   | Wako Fujifilm         | 415-73301   |
| Lipofectamine 2000 transfection reagent   | Invitrogen            | 11668019    |
| FuGENE 6 transfection reagent   | Promega               | E269A       |
| Pierce BCA protein assay kit  | Thermo Scientific     | 23225       |
| <b>Experimental Models: Cell Lines</b>  |                       |             |
| 293T cells  | ATCC                  | CRL-3216    |
| MC38-OVA cells  | John Stagg            | 68          |
| <b>Experimental Models: Organisms/Strains</b>   |                       |             |
| C57BL/6J mice   | Jackson Laboratories  | JAX:000664  |
| Tg(TcraTcrb)1100Mjb (OT-I) mice   | Jackson Laboratories  | JAX:003831  |
| CD90.1 (Thy.1.1) mice   | Jackson Laboratories  | JAX:000406  |
| B6.SJL- <i>Ptprc<sup>o</sup></i> <i>Pepc<sup>o</sup></i> /BoyJ (CD45.1) mice  | Jackson Laboratories  | JAX:002014  |
| B6.Cg-Tg(Cd4-cre)1Cwi/BfluJ ( <i>Cd4-Cre</i> ) mice   | Jackson Laboratories  | JAX:022071  |
| <i>Bdh1</i> -floxed mice  | Daniel Kelly          | 33          |
| <i>Oxct1</i> -floxed mice   | Peter Crawford        | 51          |
| <b>Oligonucleotides</b>   |                       |             |
| Firefly luciferase shRNA (LMPd-Amt backbone):<br>AGCTCCCGTGAATTGGAATCCTAGTGAAGCCACAGATGTAGGATTCCAATTC<br>AGCGGGAGCC | Matthew Pipkin        | 69          |

| REAGENT or RESOURCE   | SOURCE                                  | IDENTIFIER   |
|---|---|--|
| <i>Oxct1</i> shRNA (LMPd-Amt backbone):<br>TGCTGTTGACAGTGAGCGCCGGAAGGATGTCAGTAATCAATAGTGAAGCCAC<br>AGATGTATTGATTACTGACATCCTCCGTTGCCTACTGCCTCGGA | This paper                              | Custom   |
| <b>Recombinant DNA</b>  |   |  |
| pLMPd-Ametrine (LMPd-Amt)   | Matthew Pipkin                          | 69   |
| Lentiviral-S-tdTomato   | Addgene                                 | Plasmid #112579  |
| pCMV-VSV-G  | Addgene                                 | Plasmid #8454  |
| psPAX2  | Addgene                                 | Plasmid #12260   |
| pCL-Eco   | Steven Reiner                           | Plasmid #12371<br>(Addgene)  |
| <b>Software and Algorithms</b>  |   |  |
| FlowJo v9.9.5   | FlowJo LLC                              | <a href="http://www.flowjo.com">www.flowjo.com</a>                               |
| GraphPad Prism v9   | GraphPad Software                       | <a href="http://www.graphpad.com">www.graphpad.com</a>                           |
| Compound Discoverer v3.2  | Thermo Scientific                       | <a href="https://www.thermofisher.com/">https://<br/>www.thermofisher.com/</a>   |
| Mass Hunter v10   | Agilent Technologies                    | <a href="https://www.agilent.com">https://www.agilent.com</a>                    |
| Integrative Genomics Viewer   | UCSD/Broad Institute                    | <a href="http://www.igv.org">www.igv.org</a>                                     |
| IncuCyte v2022A Rev1  | Sartorius                               | <a href="https://www.sartorius.com/en">https://<br/>www.sartorius.com/en</a>     |
| MaxQuant v2.0.3.0   | Max-Planck Institute<br>of Biochemistry | <a href="https://www.maxquant.org/">https://<br/>www.maxquant.org/</a>           |
| UniProt   | UniProt Consortium                      | <a href="https://www.uniprot.org/">https://www.uniprot.org/</a>                  |
| Compass DataAnalysis v5.3   | Bruker Daltonics                        | <a href="https://www.bruker.com/en.html">https://www.bruker.com/<br/>en.html</a> |